Raman mapping for the investigation of nanophased materials

Gwenaël Gouadec, Ludovic Bellot-Gurlet, Denis Baron, Philippe Colomban

Chapter 3
Raman Mapping for the Investigation of Nano-phased Materials

G. Gouadec, L. Bellot-Gurlet, D. Baron and Ph. Colomban

Abstract Nanosized and nanophased materials exhibit special properties. First they offer a good compromise between the high density of chemical bonds by unit volume, needed for good mechanical properties and the homogeneity of amorphous materials that prevents crack initiation. Second, interfaces are in very high concentration and they have a strong influence on many electrical and redox properties. The analysis of nanophased, low crystallinity materials is not straigtforward. The recording of Raman spectra with a geometric resolution close to $0.5\,\mu m^3$ and the deep understanding of the Raman signature allow to locate the different nanophases and to predict the properties of the material. Case studies are discussed: advanced polymer fibres, ceramic fibres and composites, textured piezoelectric ceramics and corroded (ancient) steel.

3.1 Raman Spectroscopy and (Nano)materials Properties

Nanosized and nanophased materials possess a high concentration of interfaces, which results in unique optical and redox properties, as well as a good resistance to crack propagation. Not all conventional materials science research techniques are

G. Gouadec (✉) · L. Bellot-Gurlet · D. Baron · Ph. Colomban
Laboratoire de Dynamique, Interactions et Réactivité (LADIR), UMR 7075,
CNRS et Université Pierre et Marie Curie (UPMC - Paris 6),
4 place Jussieu, 75252, Paris, Cédex 05, France
e-mail: gwenael.gouadec@upmc.fr

L. Bellot-Gurlet
e-mail: ludovic.bellot-gurlet@upmc.fr

D. Baron
e-mail: denis.baron@upmc.fr

Ph. Colomban
e-mail: philippe.colomban@upmc.fr

A. Zoubir (ed.), *Raman Imaging*, Springer Series in Optical Sciences 168,
DOI: 10.1007/978-3-642-28252-2_3,

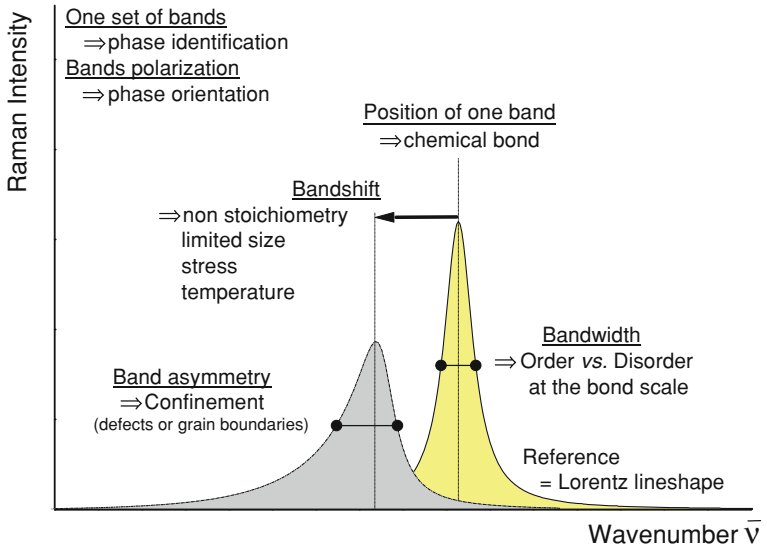

Fig. 3.1 The basics of Raman spectra interpretation. The vibrational wavenumbers are often called Raman shifts as they correspond to a Raman-induced wavenumber shift of the scattered photons with respect to the laser excitation

applicable to study the structure–properties relationship in such materials and Raman microspectroscopy (μRS) is one of them (Fig. 3.1) [1, 2]:

- The actual probes are vibrational modes, which strongly depend on atoms mass, bond lengths and the angles between atom-sharing bonds.
- In the most frequent case where a visible laser is used for the excitation (IR and UV-Raman are also possible), the excitation and collection of the signal is performed through a standard optical microscope, which makes a selection of the analysis point very easy.
- Even low crystallinity materials like those often found at interfaces (which seldom reach thermodynamic equilibrium during the synthesis process) are available for analysis.

More generally, Raman spectroscopy being a non contact, non destructive, and relatively fast technique, it offers the possibility to characterize a material under working conditions and assess how external perturbations (mechanical stress, thermal cycling, electrochemical cycling, corroding atmosphere, …) may affect it.

Modern Raman microspectrometers are equipped with motorized tables and acquisition softwares allowing for the automated mapping of a surface. The user ultimately gets a "hyperspectral map", which is a collection of individual Raman spectra, each being associated with a given point on the sample surface (Fig. 3.2). Note that *Raman mapping* must not be confused with *Raman imaging*, where a large area is lit by a defocused laser beam and photons from only one selected wavenumber

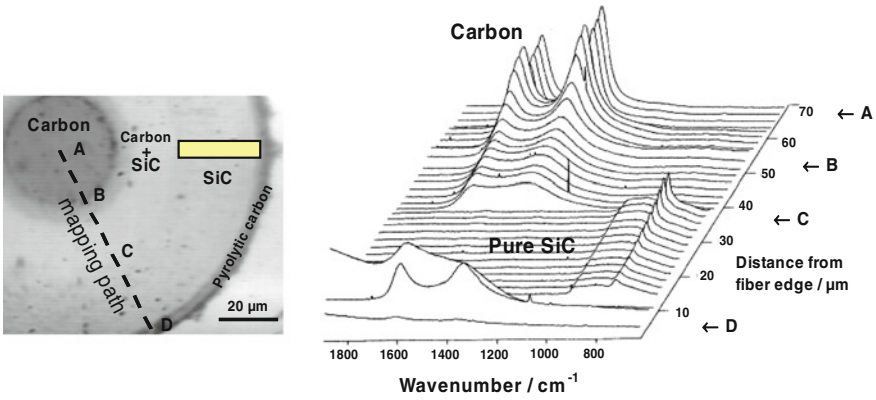

Fig. 3.2 In-line Raman map of a SCS-6 fiber radius (adapted from Ref. [6]). The *shaded rectangle* in the optical picture indicates the region mapped in Fig. 3.16

range form an image of that area on a mosaic detector (CCD) [3]. The possibility exists to use hyperspectral maps data to build a "map" of the investigated area where the color of each point indicates the integrated Raman intensity in a wavenumber Range Of Interest (ROI). Such a map may be useful to locate a phase with strong Raman scattering in the ROI (Figs. 3.3 and 3.4) but a much more sophisticated analysis is achieved with maps of spectral parameters (position, width, area or intensity of a given band) obtained through the mathematical fitting of the Raman spectra. If a physical property can be expressed as a function of one or several such parameters, it is eventually possible to draw a "smart map" [4, 5] of that property based on the treatment of Raman spectra (see for instance Figs. 3.14, 3.16–3.19, and 3.21c).

3.2 Recording a Raman Map

Raman mapping is most valuable to point out subtle spectral modifications taking place from one place of a sample to another (Figs. 3.2–3.4 and 3.17). A large number of good quality spectra are thus necessary and the overall recording time (t_{rec}) will possibly reach several hours. Some preliminary thinking is advisable to make the most of it.

3.2.1 The Lateral Resolution of µRS

First of all, the microscope objective should be chosen for the resulting probing to match the sample details of interest. From a practical point of view, microscope objectives are usually characterized by the numerical aperture NA [8]:

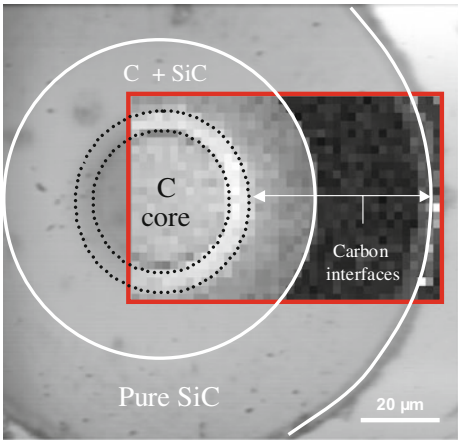

Fig. 3.3 The selection of graphite signal (ROI at 1300–1600 cm^{-1}) in a Raman map (*boxed rectangle*; 1 µm ×1 µm *square pixels*) reveals the different regions of an SCS-6 fiber (the darker a pixel, the lower the graphite signal)

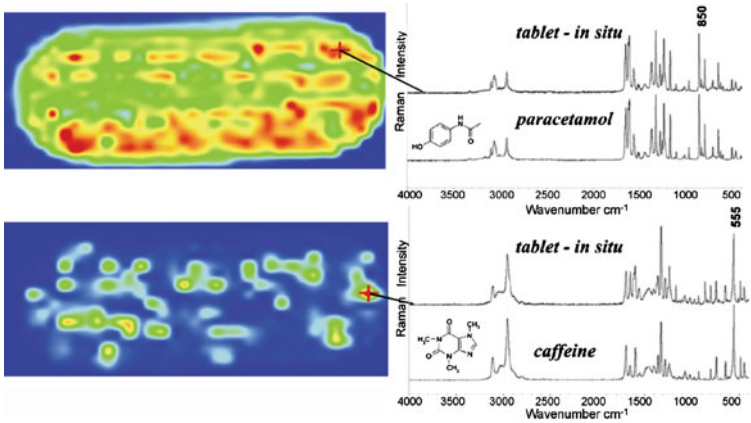

Fig. 3.4 The Raman mapping of a drug tablet (18.0 × 8.5 mm) makes it possible to discriminate paracetamol (ROI at 850 cm^{-1}) from caffeine (ROI at 555 cm^{-1}). Reprinted with permission from Elsevier [7]

$$\mathrm{NA} = n \sin(\theta_{\mathrm{back}}) \tag{3.1}$$

In Eq. (3.1), θ_{back} is the maximum collection angle for the backscattered light and n is the refractive index in the medium between the sample and the microscope lens (Fig. 3.5).

The numerical aperture is a key parameter because it sets the resolution R of the microscope, defined as the shortest spacing for two points on a sample surface to be resolved with λ wavelength observation [9]:

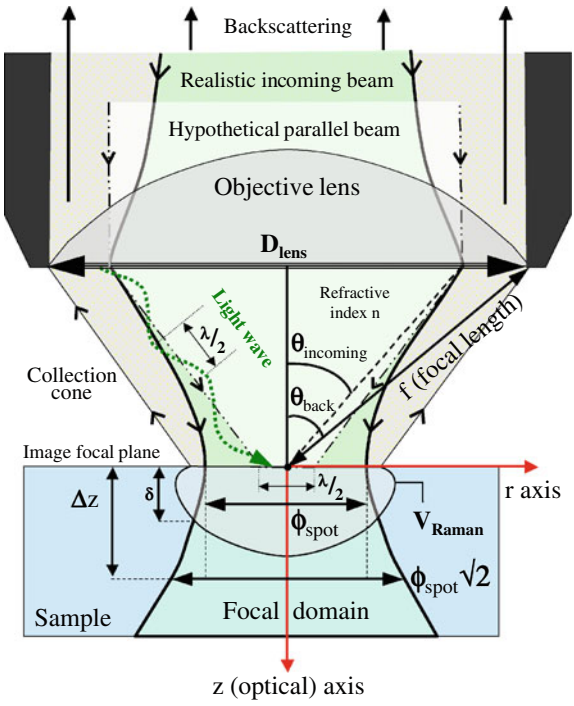

Fig. 3.5 Basic schematic of the Raman microscope in backscattering configuration. The labels signification is given throughout the text

$$R \sim \frac{0.61\lambda}{\mathrm{NA}} \tag{3.2}$$

Equation (3.2) is usually referred to as Rayleigh criterion and follows from Abbe theory of the diffraction pattern created by distinct point sources observed through a microscope [10]. The best objectives (oil immersion objectives) having numerical apertures around 1.4, Rayleigh criterion is sometimes referred to as a "$\lambda/2$ *diffraction limit*". The focusing of incoming laser beams, even perfectly parallel ones, is diffraction limited by their finite diameter. Rayleigh criterion therefore forbids to obtain a laser spot smaller than about half the laser wavelength (Fig. 3.5), even though smaller objects will still give a Raman signal. Figure 4.2 in the next chapter illustrates this last point: 170 nm diameter GaN nanowires were indeed observed with a lateral resolution of, at best, 230 nm (confocal microscope—see further; 0.9 NA; $\lambda = 514.5$ nm) [11]. Besides, the polarization sensitivity of GaN nanowires Raman modes demonstrates the possibility to analyze growth directions and crystallographic orientations in nanophases.

Actual laser beams are not perfectly parallel (which has been exaggerated in Fig. 3.5) and their focusing through a microscope lens actually gives an elongated volume, which is called the focal domain or focal cylinder [12, 13]. The diameter $\phi(z)$ of the focal domain at z axial coordinate must be defined arbitrarily as the

electric field obviously does not drop to zero for a definite r distance away from the optical axis. The radial decrease of the electric field in a laser beam actually obeys a Gaussian law and $\phi(z)$ is often taken where the maximum field $E_0(z, 0)$ is divided by e [13]:

$$E(z, r) = E_0(z, 0)e^{-4(r/\phi(z))^2}, \quad \text{with} \quad \phi_{\text{spot}} = \phi(z = 0) \tag{3.3}$$

We will assume for simplicity that the lens (focal length: f; Diameter: D_{lens}) is fully lit by the incident beam. In such conditions (the incoming beam diameter equals D_{lens} and $\theta_{\text{incoming}} = \theta_{\text{back}} = \theta$ in Fig. 3.5), it can be shown that [12, 13]:

$$\phi_{spot} \sim \frac{4\lambda f}{\pi D_{\text{lens}}} = \frac{2\lambda}{\pi \sin\theta} = \frac{2n\lambda}{\pi \text{NA}} \tag{3.4}$$

Combining Eqs. (3.2) and (3.4), one finds:

$$\frac{\phi_{\text{spot}}}{R} = \frac{2n}{0.61\pi} \sim n \tag{3.5}$$

ϕ_{spot} is thus very close to the diameter of the smallest circle in which all incoming energy can, in theory, be focused. Remember however that, according to Eq. (3.3), ϕ_{spot} delimits a zone receiving only 86 % of the total laser irradiance [13].

3.2.2 The Axial Resolution of μRS

Similar to the lateral resolution, the in-depth or axial resolution of Raman spectroscopy cannot be defined unambiguously. Indeed, the laser intensity does not drop to zero for a given z value and one has to choose an arbitrary threshold. It is common to use the *depth of field* Δz (Fig. 3.5), which is the distance along which the irradiance is cut by half (or, equivalent, ϕ(z) is multiplied by $\sqrt{2}$) [13]. Note that Raman spectroscopists often improperly refer to Δz as a *depth of focus* (which should refer to the focus tolerance in the image plane of the microscope). For the lens focusing of a Gaussian beam, one finds [12, 13] (there is a missing λ factor in Eq. (11) from Ref. [13]):

$$\Delta z \sim \frac{8\lambda}{\pi} \times \left(\frac{f}{D_{\text{lens}}}\right)^2 = \frac{2n^2\lambda}{\pi \text{NA}^2} \tag{3.6}$$

The calculation in Eq. (3.6) is based on the laser focal cylinder but the actual probing depth (δ in Fig. 3.5) can be significantly lower in absorbent materials (δ is inversely proportional to the linear absorption (or attenuation) coefficient [14]), making μRS a surface technique.

In the confocal microscopy setup, pinholes are placed in the microscope at intermediate image planes, resulting in a better in-depth discrimination power [15].

In that case, the integrated intensity coming from a given plane perpendicular to the optical axis is no longer a constant but, rather, decreases by 50 % between the focal plane ($z = 0$) and $\Delta z_{\text{confocal}}$ (the half width of the so-called point spread function), which is well approximated with [16, 17]:

$$\Delta z_{\text{confocal}} \sim \frac{4.4 n \lambda}{2\pi \text{NA}^2} \tag{3.7}$$

The use of confocal pinholes goes with a lateral resolution improvement of about one third [17] but confocal microscopy interest mainly consists in the possibility to select sample layers axially.

Note that Δz and $\Delta z_{\text{confocal}}$ should obviously not be compared as the former only considers intensity variations along the optical axis, whereas the latter is based on the total intensity distribution at a given z value. Moreover, it might seem surprising that Eq. (3.7) does not involve the confocal pinholes diameter but it is implicitly assumed to be at an optimum corresponding to R_{confocal} (the lateral resolution in confocal mode) times the total magnification (usually greater than the nominal magnification of the objective) at the pinhole image plane [18].

3.2.3 Practical Aspects of Raman Mapping

Because μRS is sensitive to chemical bonds (through their vibrations), the technique obviously provides useful information about the nano-organization of matter. However, even with the best dry ($n = n_{\text{air}} = 1$, NA $= 0.95$) or oil immersion ($n = 1.51$, NA $= 1.4$) objectives, and in the most favorable case of a blue excitation ($\lambda \sim 400$ nm), ϕ_{spot} will remain above 275 nm (Eq. 3.4). Unless nano-objects are extremely dispersed in the sample (and the signal is still strong enough for analysis, which can be obtained by Surface Enhanced Raman Scattering—SERS [19, 20]), each Raman spectrum will therefore give the average response of a very large number of nano-objects. Mathematical simulations of the spectra should then ideally include statistical distributions of size or size-governed properties [21–32].

As a matter of fact, there is a possibility to break the $\lambda/2$ diffraction limit of optical microscopes and make Raman lateral resolution nanometric by maintaining a sharp metallic tip extremely close to the sample, with micro-manipulation tools borrowed from Atomic Force and Scanning Tunneling Microscopes (AFM/STM) [33, 34]. This Tip-Enhanced Raman Scattering (TERS) became a very hot topic in the past decade but its implementation still requires too much experimental and theoretical expertise for a generalized use [35]. We shall leave TERS aside and focus on the nano-related information that can be retrieved using conventional μRS. For that matter, let us first stress that the V_{Raman} volume drawn in Fig. 3.5 to represent the region probed in the sample neither matches ϕ_{spot}, nor Δz. Equations (3.4) and (3.6) may indeed give good estimates for the lateral and axial resolution of μRS but a number of factors will affect the actual values:

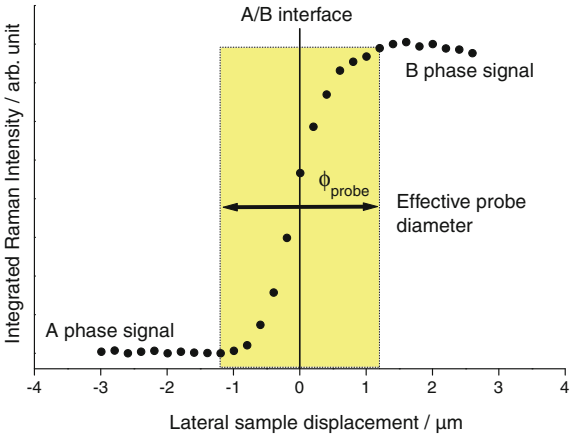

Fig. 3.6 Determination of the spatial resolution of a Raman microscope by crossing the interface between phases A and B at right angles. The wavenumber domain over which intensity is integrated must be chosen so as to maximize the difference in scattering efficiency between A and B phases

- Optical aberrations of the optical parts (lenses, mirrors, etc).
- Imperfect laser alignment along the optical axis of the microscope.
- Parasite refractions at the sample/light propagation medium interface [36, 37].
- A poor phase contrast on the sample surface.
- Light absorption in the sample (if $\delta << \Delta z$).
- Multiple scattering.

It might be advisable, especially in view of large-scale mapping campaigns, to get experimental spatial resolution values in the actual working conditions. A precise measurement of the spot diameter is easily achieved with a line-mapping across the interface of two phases (for instance a metal piece polished in a resin block) having different scattering cross-sections in a given wavenumber window [5, 38–40]. The plot of the intensity recorded in that window as a function of the displacement across the interface will resemble that shown in Fig. 3.6, thus providing the effective probe diameter ϕ_{probe}. As for the axial resolution, it can be measured from the intensity profile recorded when a mirror replacing the sample is taken away from the image focal plane of the microscope [41, 42].

3D-Raman mapping is possible in low absorbance samples or when small scatterers are dispersed in a transparent matrix [43], but 2D-raster mapping with ΔX and ΔY displacement steps of the sample-baring motorized table is much more common (Fig. 3.7a). However, if the microscope has the autofocus option, the axial degree of liberty may still serve to compensate the lack of planarity and/or horizontality of the sample surface. We shall further focus on Raman mapping with square pixels ($\Delta Y = \Delta X$, as shown in Fig. 3.7a), which obviously optimizes the sample surface coverage by a circular spot. The condition guaranteeing full probing of the mapped area (A_{map}) is:

$$\Delta X = \frac{\phi_{\text{probe}}}{C}; \quad \text{with } C \geq \sqrt{2} \tag{3.8}$$

In Eq. (3.8), $\sqrt{2}$ is the limit value for the laser spot to just reach the corners of each targeted "*pixel*" (the sample zone to which the recorded spectrum will be attached), but even in that case (mapping with ΔX_1 step in Fig. 3.7a), some part of the signal will actually come from neighboring pixels. Increasing C (decreasing ΔX) will raise the proportion of light backscattered from untargeted pixels (see the mapping with ΔX_2 step in Fig. 3.7a) but it will also improve the rendering of the sample details.

As a matter of fact, Raman intensity measured at pixel coordinate (x_p, y_p) is a convolution of the Raman scattering efficiency (σ function) by the (Gaussian) lineshape of the laser beam cross-section (half width at half maximum w):

$$I\left(\bar{\nu}, x_p, y_p\right) \propto \int\int \sigma\left(\bar{\nu}, x, y\right) \times e^{-\ln 2 \frac{(x-x_p)^2+(y-y_p)^2}{w^2}} \mathrm{d}x\mathrm{d}y \tag{3.9}$$

According to Eq. (3.9), the exact position of any heterogeneity at the surface of the mapped area (for instance the L-wide inclusion in Fig. 3.7b) will necessarily be somewhere in the pixel showing the strongest heterogeneity-related Raman contribution. Details will thus be located with a precision of ΔX. Yet, even in the limit of $\Delta X \to 0$, they will appear about as large as ϕ_{probe}. This can be understood with the situation depicted in Fig. 3.7b: the L-wide inclusion will clearly contribute to the targeted pixel even though it is located outside the region associated with the said pixel.

Only a mathematical deconvolution of the hyperspectal map by the laser lineshape will "isolate" the signal truly coming from each pixel [4, 5, 39] (Fig. 3.8) but it will not be reliable if the phase repartition changes for depths lower than the laser penetration (the case illustrated for the irregular inclusion in Fig. 3.7b). Most 2D-imaging software programs offer the possibility to interpolate data points but it is only a smoothing of the images (Figs. 3.4, 3.14, 3.16, 3.20 and 3.21), which does not actually involve any deconvolution procedure [44].

If t_{spec} is the time to be devoted to each spectrum acquisition,[1] the total number of spectra N_{spec} in a Raman map will be:

$$N_{\text{spec}} = \frac{t_{\text{rec}}}{t_{\text{spec}}} = \frac{A_{\text{map}}}{\Delta X^2} \tag{3.10}$$

And the combination of Eqs. (3.8) and (3.10) yields:

$$\phi_{\text{probe}} = C\sqrt{\frac{A_{\text{map}}\, t_{\text{spec}}}{t_{\text{rec}}}} \tag{3.11}$$

Mapping a sample with a given objective, that is to say a given ϕ_{probe} value, will involve adjusting parameters C (hence ΔX step), A_{map}, t_{spec} and t_{rec} so as to satisfy

[1] t_{spec} must include the effective acquisition time but also the time-out for the displacements of the motorized table (usually negligible) for the (optional) auto-focus sequence, for the gratings rotation (in case of multi-window recording) and for data saving.

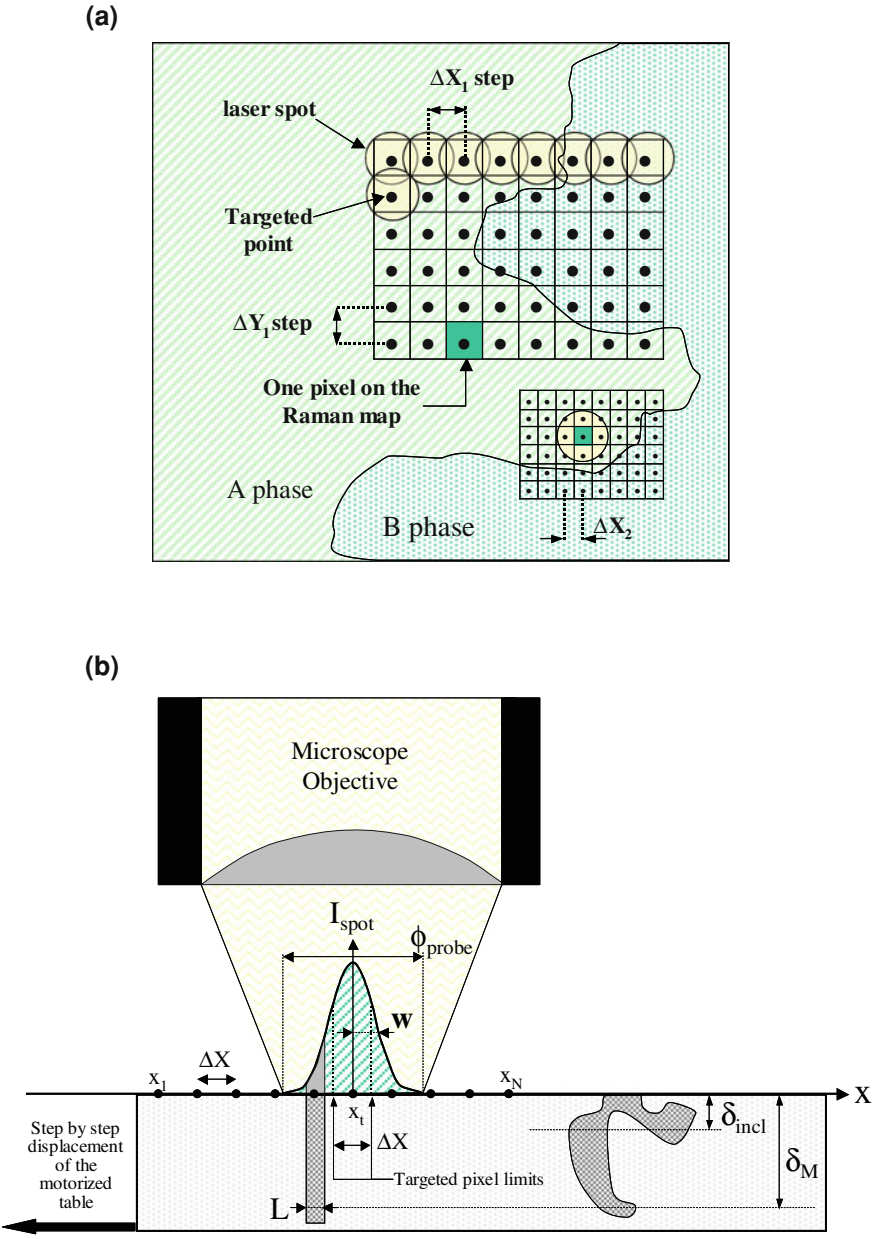

Fig. 3.7 **a** Schematic of two 8 × 6 raster mappings with square *pixels* (displacement steps $\Delta X = \Delta Y$); **b** schematic of the in-line mapping (ΔX step) of material M (laser penetration δ_M) with one L-wide and one irregular inclusions (laser penetration δ_{incl}). Each of the N spectra is attached to a ΔX-wide *pixel*. I_{spot} gives the Gaussian distribution (half width w) of the laser intensity across the experimental spot diameter (ϕ_{probe}) and all the scattering collected from the illuminated region contributes to the targeted pixel (x_t). The Raman contribution of the L-wide inclusion is proportional to the gray area below the laser intensity curve

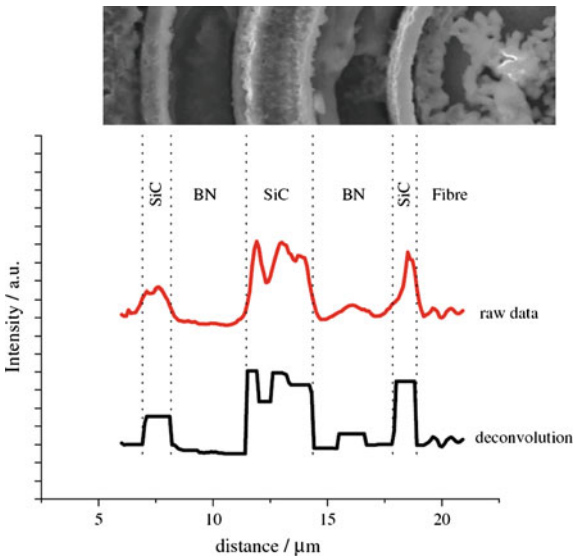

Fig. 3.8 The laser spot lineshape can be deconvoluted from the in-line Rayleigh map along the radius of a BN/SiC-covered SiC fiber in order to enhance the lateral resolution. The same procedure would apply to Raman mapping. Reprinted with permission from Elsevier [1].

Eq. (3.11). Because of the square root, increasing C (decreasing ΔX) for a given mapping time t_{rec} will involve strong concessions on the map dimension (cutting ΔX by two divides A_{map} by four; Fig. 3.7a) and/or the signal to noise ratio (reduced t_{spec}).

3.3 Data Processing

3.3.1 Spectra Simulation

The scattering of light by identical vibrators (wavevector $\bar{\nu}_c$) should result in a lorentzian-shaped band (half width γ), but most experimental lineshapes are best fitted by a convolution with a Gaussian profile (half width: $\sigma\sqrt{(2ln2)}$) representing the distribution of vibrators in slightly different states:

$$I\left(\bar{\nu}_c + \bar{\nu}\right) \propto \int_{-\infty}^{+\infty} \frac{\gamma}{\sigma} \times \frac{e^{-\left(\frac{\bar{\nu}'^2}{2\sigma^2}\right)} d\bar{\nu}'}{\left(\bar{\nu} - \bar{\nu}'\right)^2 + \gamma^2} \tag{3.12}$$

The use of simple Gaussian and Lorentzian profiles is often preferred to the Voigt profile described by Eq. (3.12) as they depend on three parameters instead of four (many fitting modules misleadingly name Voigt profile the simple sum of one Lorentzian and one Gaussian).

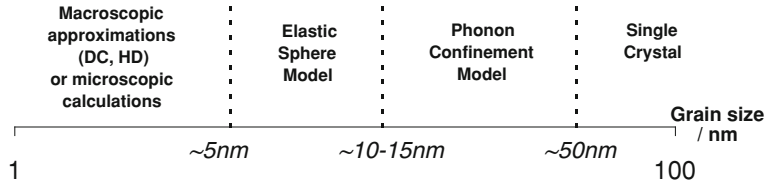

Fig. 3.9 Modeling spherical nanocrystals vibrations as a function of the grain size (Dielectric Continuum (DC); Hydrodynamic model (HD). After Ref. [1]

To the second order, the exact position, intensity, width, and lineshape of each band depend on many different parameters [1, 45] such as neighboring defects (inclusions, substitutions, or vacancies) [46–51], grains size and shape [25, 52–61], phase orientation (polarization effects [11, 62–66]), or thermomechanical stress (anharmonic effects) [67–71] (Fig. 3.1). Taking full benefit of the available information thus requires some critical interpretation of the raw spectra and an adaptation of standard fitting procedures to the specific case under focus. For instance, different models may be necessary to correlate Raman spectra to grain size (Fig. 3.9):

- In grains much larger than the wavelength, phonons propagate almost in the same way as in perfect "infinite" crystals.
- When the grain size falls in the tens of nanometer range, the Phonon Confinement Model (PCM; see Sect. 3.3.2) accounts for the phonon coherence length limitation by a weighed integration of the optical dispersion curves from Brillouin zone center outwards [1, 72, 73].
- Below a certain size, the very notion of collective vibrations disappears and the Elastic Sphere Model (ESM) takes over, using first principle description of low wavenumber vibrations in a "free-standing" sphere of a homogeneous (constant density) elastic medium [1, 74–78]. In this scheme, the Raman wavenumber values are inversely proportional to nanoparticles diameter [1, 77, 79, 80].
- In semiconductor quantum structures too small to be seen as homogeneous, macroscopic approximations taking the geometry of the sample into account by mechanical and/or electrostatic boundary conditions (the so-called dielectric continuum and hydrodynamic models, with all their modified versions) can be used [56, 81–86].

3.3.2 "Blind" Data Processing

In the (unfavorable but frequent) case when one has no preconceived idea about the Raman parameters most relevant to a specific issue, the comparison of spectra recorded on different samples and/or for different conditions is necessary. If nothing appears at first sight, a chemometric analysis might prove very useful. The main

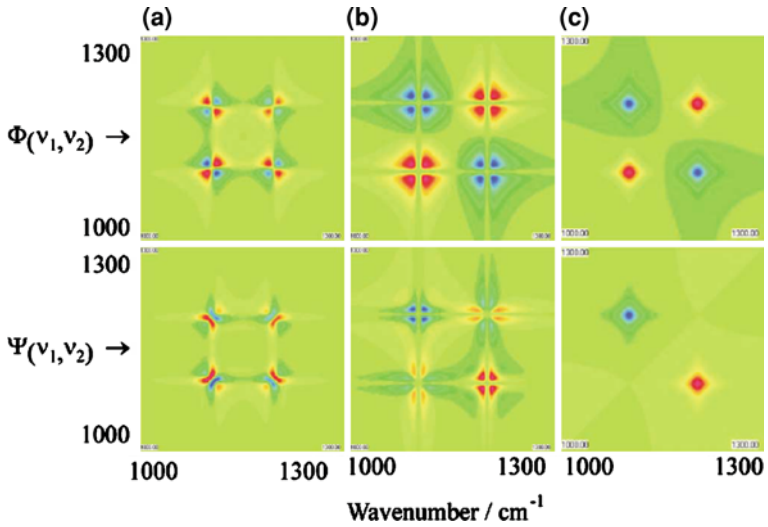

Fig. 3.10 Synchronous (*top*) and asynchronous (*bottom*) 2D-correlation for "model" 20 cm^{-1}-wide bands at 1100 and 1200 cm^{-1} having opposite wavenumber (**a**), width (**b**), or intensity (**c**) variations. The 1100 cm^{-1} peak shifts up by 10 cm^{-1}, widens by 2 cm^{-1} and rises in intensity by 50 %. Reprinted with permission from Elsevier [92].

option is to use statistical multivariate analysis (principal components analysis, factor analysis, … [87]) to isolate the linear combinations of spectral features changing the most from one spectrum to another (the so-called *principal components*). These well-documented methods are very valuable to tell whether different samples should be connected or not but two-dimensional correlation (C2D) is a good alternative if one is interested in the effect of a given physical parameter p (which can be time but also temperature, pressure, voltage, …) on a given sample [88, 89]. Supposing that spectra I($\bar{\nu}$,p) are recorded from $p_{\min}$ to $p_{\max}$, the synchronous and asynchronous components of the spectra bidimensional correlation (Fig. 3.10), respectively $\Phi\,(\bar{\nu}_1, \bar{\nu}_2)$ and $\psi\,(\bar{\nu}_1, \bar{\nu}_2)$, are obtained through the following calculation:

$$\Phi\,(\bar{\nu}_1, \bar{\nu}_2) + i\,\psi\,(\bar{\nu}_1, \bar{\nu}_2) = \frac{\int_0^{\infty} \mathrm{FT}\,[I\,(\bar{\nu}_1,\, p)] \times \mathrm{FT}^*\,[I\,(\bar{\nu}_2,\, p)]\,\mathrm{d}P}{\pi\,(p_{\max} - p_{\min})} \tag{3.13}$$

In Eq. (3.13), FT designate Fourier transform, P being the conjugate variable of p parameter. The level curves of $\Phi\,(\bar{\nu}_1, \bar{\nu}_2)$ and $\psi\,(\bar{\nu}_1, \bar{\nu}_2)$ give a bi-dimensional representation of the correlated spectral features: Any local maximum on ϕ diagonal ($\bar{\nu}_1 = \bar{\nu}_2$) indicates a p-driven band shift, whereas off-diagonal extrema ($\bar{\nu}_1 \neq \bar{\nu}_2$) indicate coupled variations in $\bar{\nu}_1$ and $\bar{\nu}_2$ (a positive (negative) sign corresponding to variations proceeding in the same (opposite) direction). If $\Phi\,(\bar{\nu}_1, \bar{\nu}_2) \times \psi\,(\bar{\nu}_1, \bar{\nu}_2)$ is positive, then the signal starts changing in $\bar{\nu}_1$ "before" (i.e. at lower p value) it does in $\bar{\nu}_2$ (and conversely).

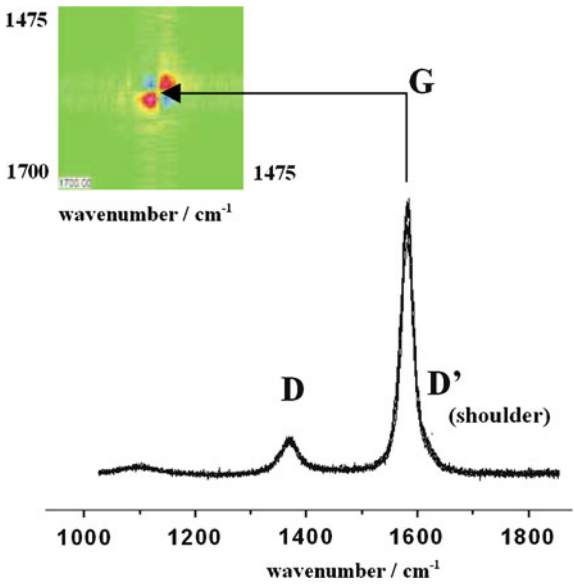

Fig. 3.11 Six spectra of an FT700 carbon fiber strained from 0.093 to 0.533 % ($\lambda_{laser} = 457.9$ nm) and the corresponding synchronous component of a 2D-correlation treatment. After [92]

2D-correlation should in theory apply to as-recorded spectra. Yet, baseline fluctuations and noise variations generate typical "streak-like" features and a baseline subtraction improves the results. The interpretation becomes even simpler if spectra are normalized prior to the calculations [90, 91]. Figure 3.10 shows the C2D spectra for two "model" bands at 1100 and 1200 cm^{-1} having opposite variations in wavenumber, width, or intensity. Intensity fluctuations give circular "halos" whereas width changes give "butterfly wings"-like features. As for wavenumber fluctuations, they can easily be recognized by crossing "egg timers" (of opposite signs) on the synchronous component and crescent-shaped features on the asynchronous one. The main limitation of C2D is that unless p is applied harmonically, there is no quantitative information associated with the values of $\Phi(\bar{\nu}_1, \bar{\nu}_2)$ and $\psi(\bar{\nu}_1, \bar{\nu}_2)$. Yet, the technique is very sensitive to the smallest variations. A very didactic illustration is provided with the spectra of a carbon fiber strained uniaxially (Fig. 3.11). There is little apparent effect of straining on the wavenumbers but the synchronous C2D function clearly shows a shift of G band.

3.3.3 "LADIR-PARADIS" Program

The proprietary softwares of Raman spectrometers manufacturers allow for hyperspectral maps mathematical treatment but many do not allow for the use of distinct models depending on the region of the map under consideration. Yet, the goal of

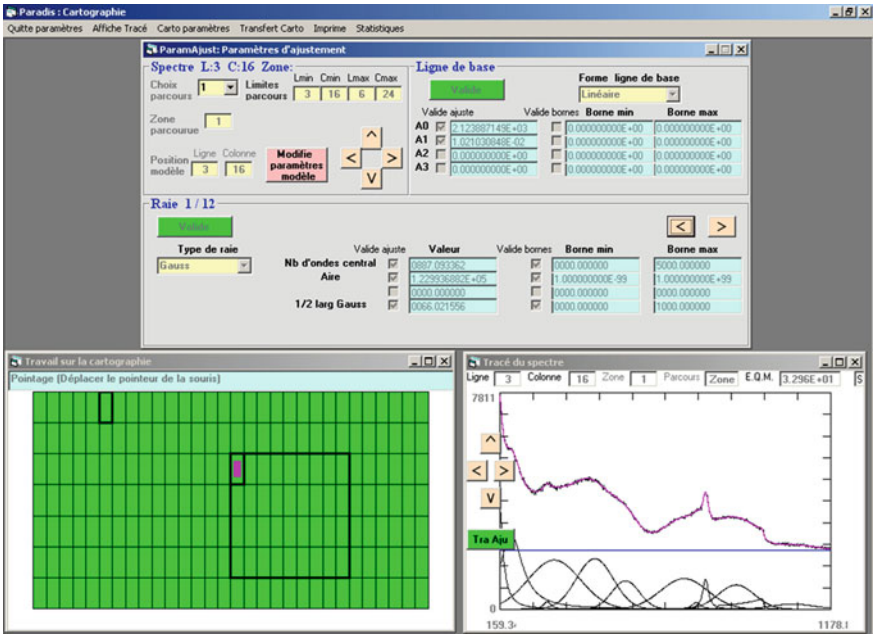

Fig. 3.12 The mapping module in "LADIR-PARADIS" program. Each pixel in the *lower left* window corresponds to one spectrum. The other two windows show the mathematical adjustment (*lower right*) and band parameters (*top*) of the active spectrum (in *pink*). Spectra in the 1×1 and 9×4 boxes were fitted with specific models

Raman mapping being to point spectral variations, a predefined model may not apply equally well to all spectra, especially if different phases are probed.

This led us to write the "LADIR-PARADIS" program (the French word for paradise is an acronym for "Programme d'Ajustement de RAies Destiné à l'Imagerie de Surfaces"—"Peak adjustment program devoted to surface mapping").[2] The opening window is very similar to what most programs offer, with the possibility to choose a baseline form and input as many bands as wanted for a spectrum adjustment. The parameters of the bands (lineshape, starting width, starting height, and starting center) are set individually and a fit using the Levenberg-Marquardt algorithm can then be launched (there is a possibility to restrict the variations of each spectral parameter between preset values). If a fitted spectrum has been chosen from a map, it can be saved as a model for the global treatment of any hyperspectral map. One specificity of "LADIR-PARADIS" is to include phonon confinement-based fits (see further; Sect. 3.3.2) but its true originality lies within the mapping window (Fig. 3.12):

- the pixels take different colors depending on the correlation factor between the adjusted and experimental spectra (green = good adjustment, red = unsatisfactory adjustment, black = aborted adjustment)

[2] This program is available from the authors.

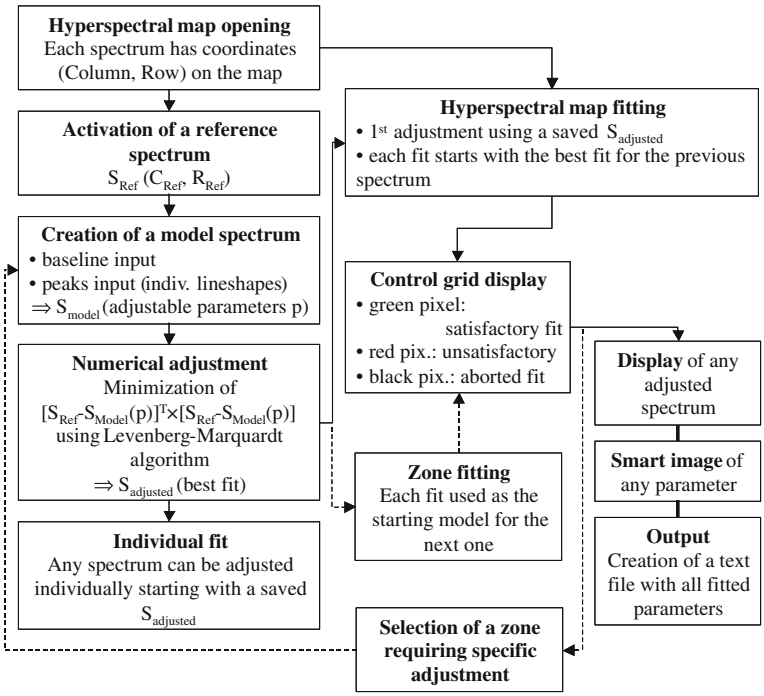

Fig. 3.13 LADIR-PARADIS program working chart

- it is possible to readjust all spectra from any area using a "local" model file (Figs. 3.12 and 3.13).

3.4 Case Studies

3.4.1 Raman Mapping of Carbon in SiC Fibers

Most natural and synthetic fibers exhibit radial structural and compositional variability. Hence the need for cross-sectional mapping which, considering a typical diameter in the range of tens of micrometers, can be easily done by μRS.

Graphite (sp^2 hybridization) has doubly degenerate E_{2g} modes at 42 and 1582 cm^{-1}. The latter is referred to as G band and corresponds to vibrations in the graphene planes. Additional modes called D and D′ (the letter stands for "disorder") appear in the Raman spectra whenever flaws are created, grain size is reduced or graphene planes are curved (Fig. 3.11). Thomsen et al. showed that only a double resonance mechanism can rigorously account for the D band [93] but an empirical

relation linking its intensity to the size of graphitic domains (L_g) has been used since 1970 [94]:

$$\frac{I_{D^{1350\text{cm}^{-1}}}}{I_{G^{1580\text{cm}^{-1}}}} = \frac{C\,(\lambda)}{L_g\,(\text{nm})}; \quad C\,(\lambda = 514.5\,\text{nm}) = 44 \tag{3.14}$$

Figure 3.14 gives an example where Eq. (3.14) was used to measure the size of carbon moieties (at the limit of the validity range [95]) on the cross-section of a silicon carbide fiber.

3.4.2 Raman Mapping of SiC in SiC Fibers

The Phonon Confinement Model (PCM) was originally proposed to describe the selection rule breaking for phonons confined in isotropic nanospheres of diameter L [72, 73]. It was later adapted to specific cases such as non isotropy [47, 96], size distribution [25, 47], or non spherical shapes (for instance in nanowires and slabs [52, 54, 55, 97]) but we shall present the original approach.

Taking k_{BZ} as the edge of Brillouin zone, q as the reduced wavevector ($0 \leq q = k/k_{BZ} \leq 1$), and assuming isotropic mode dispersion, the Raman intensity is modeled with a weighed integration of dispersion curves $\bar{\nu}_{\text{disp}}(\text{q})$:

$$\text{I}(\bar{\nu}) \propto \int_{q=0}^{q=1} \text{d}q \times \frac{\text{e}^{-\text{C}_0 \text{k}_{\text{BZ}}^2 (\text{q}-\text{q}_0)^2 \text{L}^2}}{\left[\bar{\nu} - \bar{\nu}_{\text{disp}}(\text{q})\right]^2 + \left(\frac{\Gamma_0}{2}\right)^2} \tag{3.15}$$

In Eq. (3.15), Γ_0 is the natural Raman linewidth and C_0 governs the confinement strength [52].

The PCM does not apply to acoustic modes (their energy is nil at Brillouin zone center) and is very seldom used with Transverse Optical (TO) modes (on account of their low dispersion). Because the Longitudinal Optical (LO) branches usually reach their maximum frequency at the Brillouin zone center, the integration in Eq. (3.15) introduces contributions on the low frequency side of Raman modes and the resulting peaks are asymmetrical (Fig. 3.1).

"LADIR-PARADIS" program offers the possibility to adjust the Raman bands using Eq. (3.15). The fit returns q_0 and L values based on dispersion curves of the form given in Eq. (3.16) [73], but the program could easily be adapted to alternative expressions [54, 55, 97, 98].

$$\bar{\nu}_{\text{disp}}(\text{q}) = \sqrt{A + \sqrt{A^2 - B\,(1 - \cos\pi q)}} \tag{3.16}$$

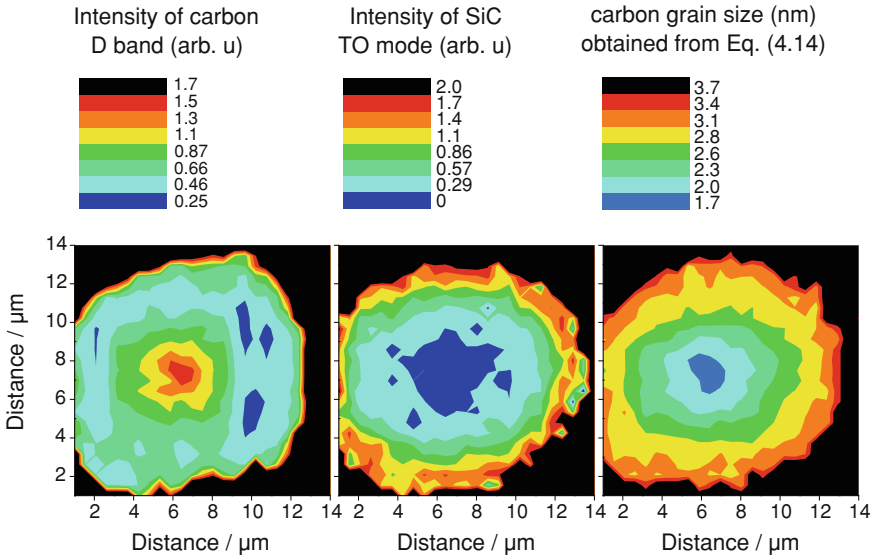

Fig. 3.14 Smart Raman maps (25 × 25 spectra) of the cross-section of an SA3 SiC fiber after 10 h-annealing at 1600 °C in reducing atmosphere (see Refs. [99, 100] for details)

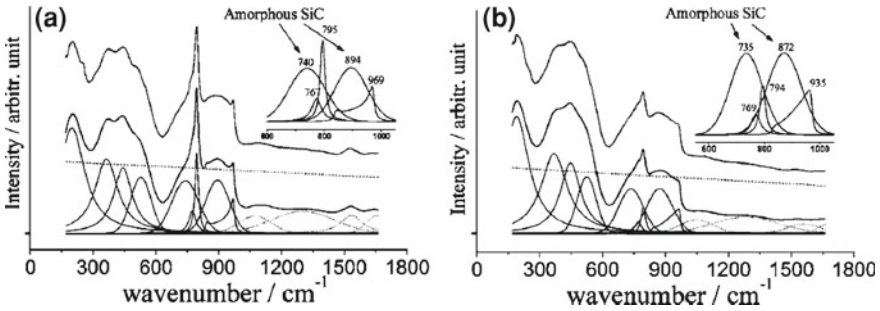

Fig. 3.15 Examples of SiC spectra fitted with a combination of Lorentz, Gauss, and "PCM" bands. The spectra were recorded at the inner (**a**) and outer (**b**) limits of the "pure SiC" region visible in Fig. 3.2. "With permission from Springer Science+Business Media: [101], figure N°6"

Figure 3.15 shows the frontier spectra of the "pure SiC" region pointed in Fig. 3.2. Their TO and LO contributions at ~795 and 970 cm^{-1} were fitted with the PCM. Note that a significant contribution from amorphous SiC was also present.

The physical interpretation of L parameter is a key element of the PCM as the phonon coherence length may either correspond to an actual grain size [24, 72, 102, 103] or to the size of any homogeneous domain limited by defects/impurities [48, 73, 104–110]. Carles et al. even showed in Ge_xC_{1-x} films that L corresponded to the actual particle size for diameters above ~20 nm but characterized domains where alloying had taken place in smaller ones [96].

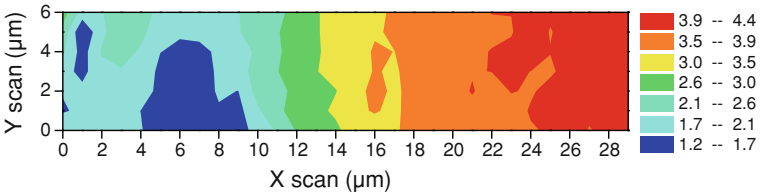

Fig. 3.16 Smart map of the Phonon Confinement Model L parameter (in nm unit) after mathematical adjustment (Eqs. 3.15 and 3.16) of the rectangular mapping from Fig. 3.2 in the SiC-rich region of SCS-6 fiber. Adapted from Ref. [101]

The L values calculated using the PCM in Fig. 3.16 are almost two orders of magnitude smaller than the diameters of the nanocrystals observed by TEM in the same region of the SCS-6 fiber [111]. The phonons appear to be confined by some free carbon in this slightly non stoichiometric region [111, 112]. In the SA-3 fiber however, the calculated L value corresponds to SiC domains extension and is unaffected by the many stacking faults appearing in TEM [113].

Disorder and nanometric dimensions often contribute to phonon confinement and their relative contributions can theoretically be isolated whenever $q_0 \neq 0$ is allowed in Eq. 3.15:

- Disorder disturbs short range order and results in Brillouin zone folding. q_0 should then stand away from Brillouin zone center and L will be inversely proportional to the density of defects.
- If the confinement takes place in perfectly ordered nanocrystals, then the activated modes should be centered at the Γ point ($q_0 = 0$) and L will represent the grain size.

3.4.3 In situ Micro-Raman Extensometry of Fibers and Fiber-Reinforced Composites

Because bonds vibrations have some anharmonic character, Raman bands have a tendency to shift in materials submitted to external stress ([1] and references therein). In perfect crystals, symmetry considerations make Raman bandshifts simple linear combinations of the stress tensor components [114–116]. Conversely, if several Raman bands are observed simultaneously and/or simplifying assumptions are made on the stress state, the latter can be measured from experimentally observed band shifts (Fig. 3.17) [41, 42, 69, 117–119].

In nano/polycrystalline or amorphous materials, there is no direct relationship between bonds straining, which commands Raman shifts, and the macroscopic stress field. Yet, if one (or several) direction is made particular by the geometry of the sample, empirical calibrations of stress-induced shifts remain possible. This is the

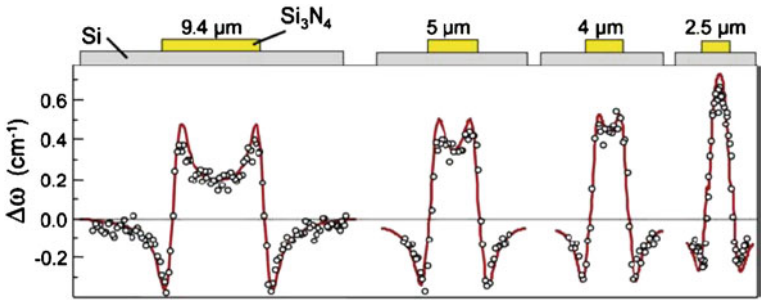

Fig. 3.17 The experimental measurement of Raman shifts in silicon (*points*) can be fitted with a stress-parameterized model (*lines*) taking into account the compression induced by silicon nitride, the laser probe diameter, the penetration depth, etc. Reproduced with permission from Wiley-Blackwell [119]

principle of Raman microextensometry (μRE) technique, which was mainly applied to fiber-reinforced composite materials. In these composites, the fibers are expected to resist axial tensions transferred from the surrounding matrix through interfacial shear stress. Their mechanical characterization therefore calls for a non destructive *in situ* measurement of the fiber axial stress [67, 68].

The first step is to calibrate the S^{ε} and S^{σ} factors linking the wavenumber shift of any specific band to, respectively, the axial strain (ε_f) and axial stress (σ_f) applied to a free-standing fiber (Young's modulus E_f; radius r_f):

$$S^{\varepsilon} = \frac{\bar{\nu}_{\text{vib}} - \bar{\nu}_{\text{vib}}^{\text{no strain}}}{\varepsilon_{\text{f}}} = E_{\text{f}} \times \frac{\bar{\nu}_{\text{vib}} - \bar{\nu}_{\text{vib}}^{\text{no strain}}}{\sigma_{\text{f}}} = E_{\text{f}} \times S^{\sigma} \tag{3.17}$$

The in situ analysis of a similar fiber through a polymer matrix (or a thin ceramic matrix layer [120, 121]) can then be used to estimate the axial stress in an embedded fiber. A mapping along the fiber axis gives a strain profile ε_f (l) from which the Interfacial Shear Stress τ (ISS), a key element in the damage tolerance of composites, can be derived :

$$\tau = -E_{\text{f}} \frac{\text{r}_{\text{f}}}{2} \left[\frac{\text{d}\varepsilon_{\text{f}}(l)}{\text{d}l} \right] = -\frac{\text{r}_{\text{f}}}{2} \left[\frac{\text{d}\sigma_{\text{f}}(l)}{\text{d}l} \right] \tag{3.18}$$

The microdroplet test (where a matrix droplet is deposited and dried on a fiber) provides the simplest way of actually preparing a sample and measuring the interfacial shear stress for a given fiber/matrix system [122–124] (Fig. 3.18a). The interfacial to axial stress ratio measures how well the stress will transfer to the reinforcing fiber in a true composite. Its diminution for increasing strains results from the degradation of the fiber/matrix interface. A number of "in line" Raman mappings have been performed to measure axial stress and ISS in polymer-embedded fibers [68, 125–127, 129–132]. Figure 3.18b shows an example for the in-line mapping of an aramid fiber reinforcing an epoxy matrix strained to 1.7 % [131]. The horizontal

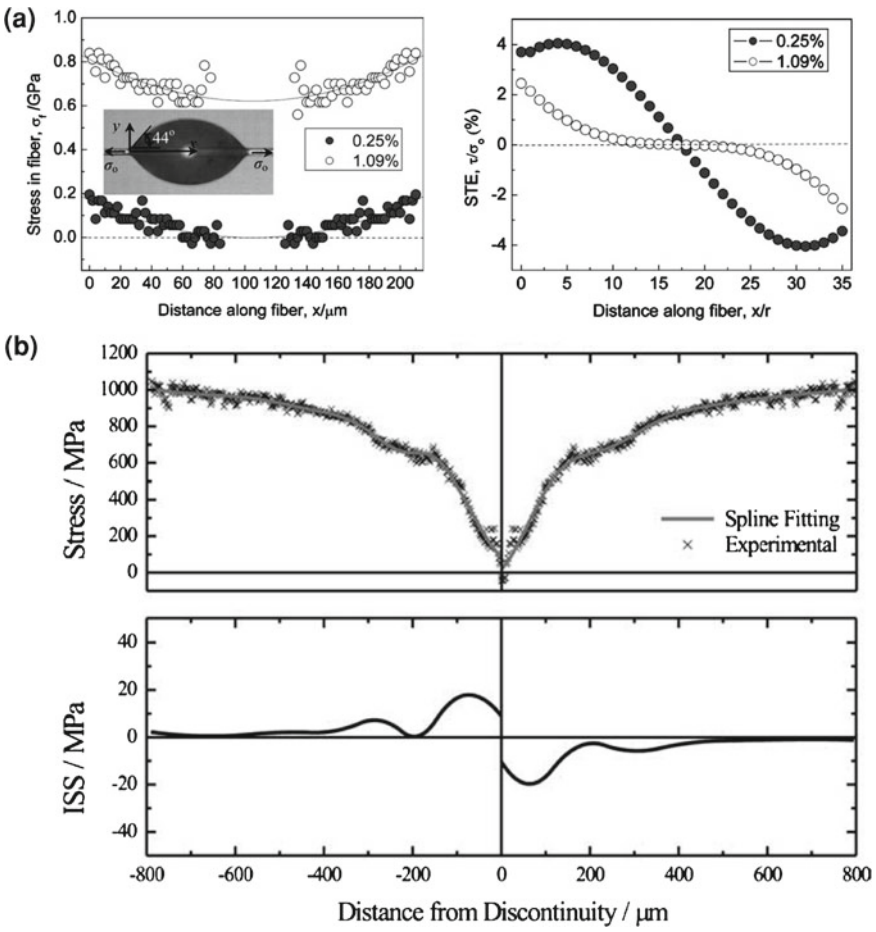

Fig. 3.18 The wavenumber shift of Kevlar-29 fiber 1610 cm^{-1} Raman peak was measured through **(a)** epoxy droplets (at 0.25 or 1.09 % fiber strain) and **(b)** the epoxy matrix of a 1.7 %-strained uniaxial composite. The fiber axial stress (σ_f) was then derived from preliminary calibrations and converted into the interfacial shear stress (ISS or τ) using Eq. 3.18. The τ/σ_f ratio measures the stress transfer efficiency (STE). Reprinted with permission from Elsevier [124] and [131]

axis origin corresponds to a fiber break where the nil stress results from full debonding. The ineffective length, over which the stress supported by the fiber builds up from zero (at a fiber tip or a matrix crack) to its maximum value, is around 400 μm.

Because the Raman signal of Carbon NanoTubes (CNTs) shifts under axial stress [133], these nanotubes were investigated as possible small dimension embedded stress gauges in the vicinity of weakly scattering reinforcing fibers (Fig. 3.19) [134–136] or in composites directly reinforced with CNTs [136, 137]. More generally, Raman spectroscopy is a lead technique for the analysis of CNTs [1, 138, 139] because a CNT is formally obtained by rolling the $n\mathbf{a}_1 + m\mathbf{a}_2$ vector of a graphene

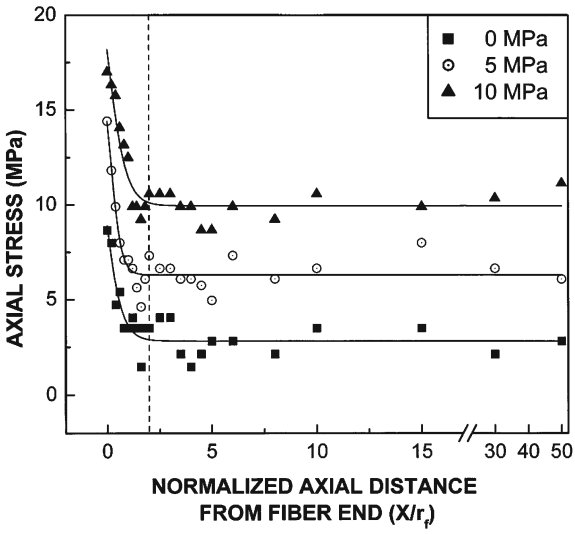

Fig. 3.19 The axial stress along a glass fiber was measured in an epoxy matrix stressed to 0, 5, and 10 MPa based on the band shifts of embedded CNTs Raman scattering (nil abscissa = fiber end). Reprinted with permission from Elsevier [135]

plane (n and m two integers; $\mathbf{a}_1$ and $\mathbf{a}_2$ basal lattice vectors) and each $\{n, m\}$ set, which relates to properties such as the tube diameter or the electrical properties (metallic vs. semiconducting), resonates for a specific excitation wavelength.

3.4.4 Raman Mapping of Micro-Indented Samples

Microindentation load-displacement curves are used to measure mechanical properties such as hardness (defined according to the indenter geometry), Young's modulus, strength, plasticity, etc. The stress can reach very high values locally (as evidenced through wavenumber shifts) and the Raman study of micro/nano-indentations is a possible way of monitoring phase transitions under non hydrostatic stress [140, 141]. Mapping capabilities are a great asset as the pressure conditions vary from one point to another (the imprints dimensions are in the range of a few tens of micrometers) because of the imperfect geometry of the indenters, the possibility of intragranular versus intergranular indentation, crack propagation at the imprints corners, materials pileup at the imprint periphery, etc., [38, 44, 141–148].

Figure 3.20 illustrates the Raman mapping of a Vickers microindentation in ZnSe. The indenter pyramid shape is easily recognized from the intensity variations (Fig. 3.20c; the deeper the imprint, the lower the intensity collected with a focus on the sample surface plane) but the wavenumber shifts are random, indicating a very inhomogeneous stress repartition in the imprint [149].

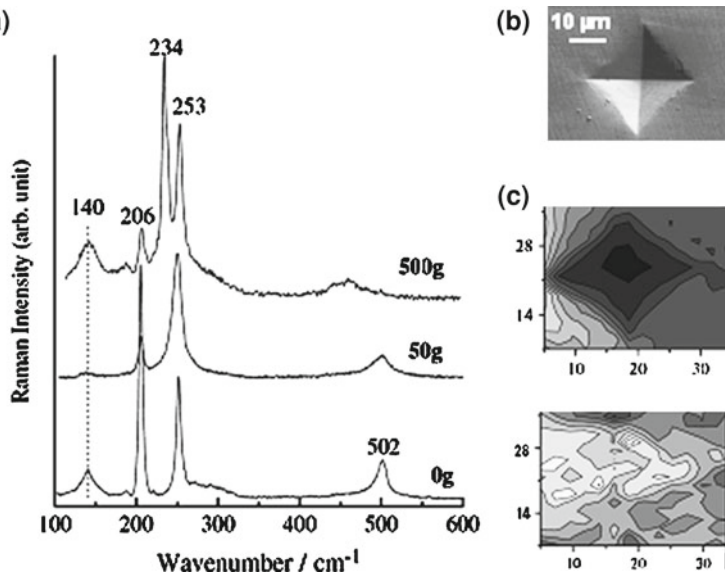

Fig. 3.20 **a** Raman spectra of ZnSe indented with a Vickers pyramid-shaped diamond micro-indenter ($\lambda_{laser} = 632.8\,nm$); **b** Micrograph of the indenter imprint after 50 g loading; **c** Intensity variation (*top*) and wavenumber shifts (*bottom*) of the 206 cm^{-1} peak on the map of (**b**) imprint (X- and Y- scales in µm). Adapted from Ref [149]

3.4.5 Metal Corrosion Layers

Raman spectroscopy is interesting for the study of corrosion because the technique has a strong sensitivity to metal-corroding anions bonds. Raman scattering allows for a phase selective microscopic scale characterization [150, 151], with the additional advantages of easy implementation, minimal sample preparation and imaging possibilities [152]. Corrosion spots may even be observed through coatings such as paint.

The observation and characterization of ancient artefact corrosion products is a key to judging the validity of long-term corrosion models since laboratory accelerated corrosion testing does not simulate long-term corrosion properly [153]. The nature and extent of long-term corrosion processes in metal-based cultural heritage objects and monuments is strongly influenced by the environment (usually soils or the atmosphere) they have stayed in [154] and a better understanding of the mechanisms at play will lead to new corrosion diagnostics tools, to improved restoration treatments, or to propose alternative conservation strategies. The possibility to predict corrosion progress will also be very helpful in view of considering iron for nuclear waste storage overcontainers.

In the specific frame of a study on the indoor atmospheric corrosion of iron, a "qualitative" Raman-based localization of corrosion phases was achieved [155].

Each phase was detected either directly through the integrated intensity in a specific ROI or, on occasion, through the ratio of intensities integrated in two ROIs. This led to images such as those shown in Fig. 3.21b. For each phase, the color levels were user-adjusted to highlight the regions of higher content but gave no indication on the phase proportion relative to the others. This approach was sufficient to describe the corrosion layers organization but a "quantitative approach" was needed, in addition to the characterization of each phase reactivity [156, 157], in order to propose quantitative diagnosis indexes [158] and confront predictive corrosion models. "LADIR-CAT" (for "Corrosion ATmosphérique"—"ATmospheric Corrosion") program was thus developed for the treatment of Raman corrosion layer hyperspectral maps [159], following a strategy initiated at LADIR for the quantitative study of organic molecule redox conformers [160] and wool dye mixtures [161]: each spectrum is fitted by a linear combination of spectra previously recorded under strictly similar conditions on pure reference phases. The different intensities of the references thus account for the difference in Raman scattering efficiency and light penetration of the different phases. This approach circumvents the difficulty (specially for solids) of calibrating the Raman intensity versus concentration relationship, which is mandatory when spectra are adjusted from normalized references [162]. However, it implicitly assumes the phase distribution is invariant along the whole investigated thickness (see Sect. 3.2.2 and discussion of Eq. 3.9 in Sect. 3.2.3).

Figure 3.22 gives an example of "LADIR-CAT" fitting and Fig. 3.23 presents the general working scheme of the program, which returns two kinds of data:

- One matrix for each phase, with as many columns and rows as there are respectively X and Y pixels in the Raman map. The number in each cell represents the calculated phase percentage for the corresponding pixel. Each matrix can be opened in a commercial software for a 2D contour fill plotting (Fig. 3.21c).
- A table giving the average percent content of each phase over the whole map, which can be presented in the form of a sector diagram (Fig. 3.21a).

LADIR-CAT was successfully used to map nine samples from the reinforcing chains of the Amiens cathedral (fifteenth century) and propose a quantitative estimation of phase composition in the corrosion system [158].

3.4.6 Raman Mapping of Biological Samples

When too many scatterers contribute to micro-Raman spectra for any one of them to be tracked, which is typically the case in samples of biological interest (lipids, proteins, carbohydrates, nucleic acids, etc., are probed simultaneously), a selectivity can be achieved with specific signal enhancers (SERS). A Raman mapping then becomes possible, as illustrated in Fig. 3.24 and in-vivo analysis possibilities were even demonstrated in small animals [163]. Because of the signal complexity in biological samples, a multivariate statistical analysis might prove useful for the analysis of Raman maps [164].

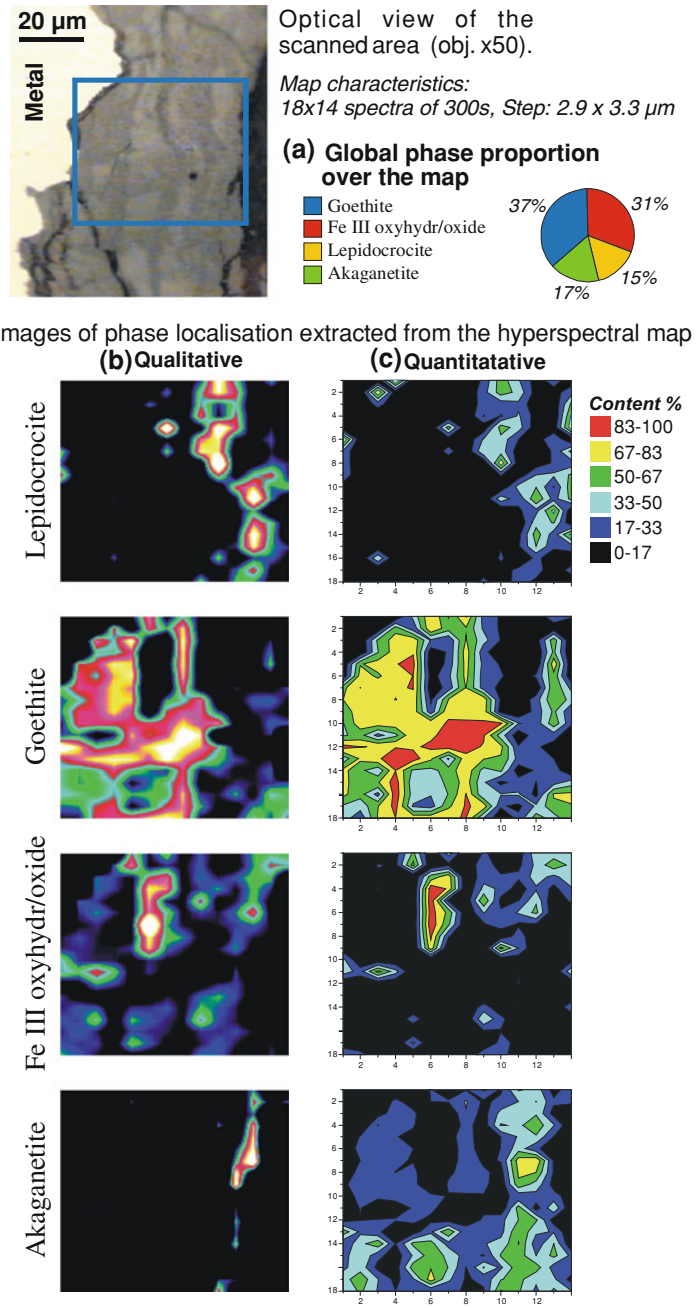

Fig. 3.21 Raman structural mapping of the indoor atmospheric corrosion layer of a sample from Amiens Cathedral. **a** the overall phase repartition, **b** "qualitative" phase mapping (based on regions of interest), and **c** quantitative results obtained from spectral decomposition by "LADIR-CAT" program

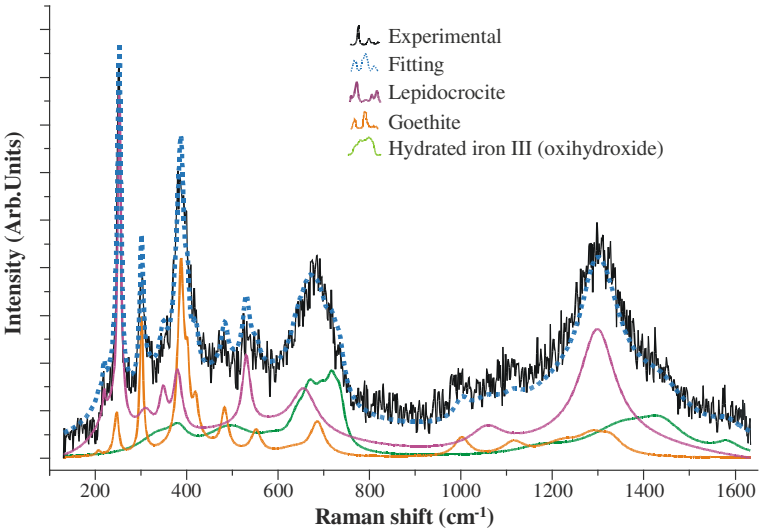

Fig. 3.22 One spectrum ($\lambda_{laser} = 514.5\,nm$, objective $\times 100$, laser power $= 100\,\mu W$, 300 s) taken from the hyperspectral map of the corrosion layer of one iron reinforcing chain in Amiens cathedral. "LADIR-CAT" program was run to adjust the data with a combination of three reference phase spectra

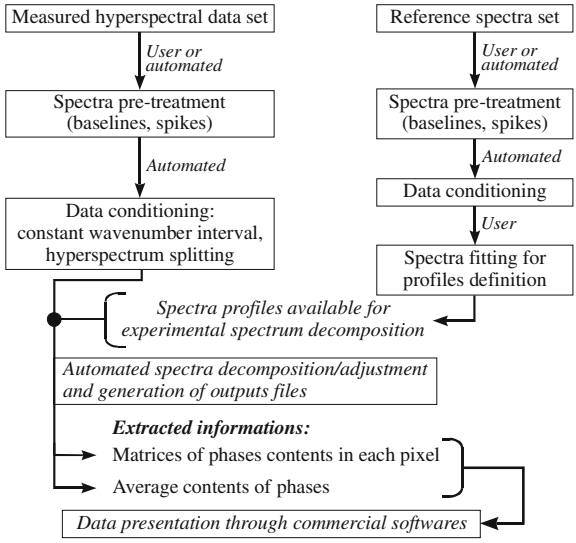

Fig. 3.23 Working scheme of "LADIR-CAT" application for automated quantitative treatment of Raman maps by the decomposition of the spectra set

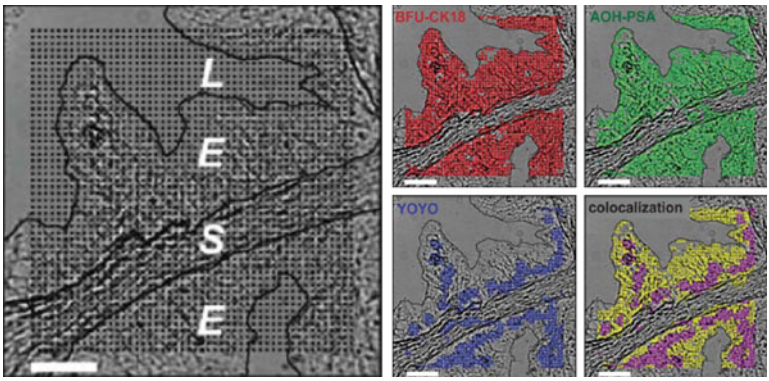

Fig. 3.24 532 nm-excited Raman scattering was recorded in XY-raster pattern (50 × 50 micrometers) over a tissue section spanning some stromal tissue (S) and prostate glands epithelia (E) or lumen (L). The sample had been stained with **i)** CK18 and PSA antibodies-conjugated Composite Organic–Inorganic Nanoparticles (COINS) associating silver (for resonance enhancement) with either basic fushin (BFU) or acridin orange (AOH) Raman labels; **ii)** DNA-specific YOYO® fluorescent dye. Localization images were obtained after applying thresholds to each probe weight in a spectral deconvolution based on reference spectra. The colocalization image identifies epithelial nuclei (*magenta*) and coexpression of CK18 and PSA specifically in the epithelium (*yellow*). Scale bars, 10 microns. Adapted, with permission from American Chemical Society [165]

3.5 Perspectives

Raman micro-spectroscopy with mapping capabilities offers great promise for fast and non-destructive analysis of various nanophased samples. From a technical point of view, the lateral resolution (about 1 square micrometer) will probably increase in the future with new objectives (×200 magnification) and tip-enhancement heads. However, the automated recording of hyperspectral maps is advantageous only if the large amount of data generated can be processed at once. Existing software packages provide a number of data treatment options but the possibility for users to write their own procedures would probably greatly improve the versatility of the method.

References

1. G. Gouadec, Ph Colomban, Raman spectroscopy of nanomaterials: how spectra relate to disorder, particle size and mechanical properties. Prog. Cryst. Growth Charact. Mater. **53**, 1–56 (2007)
2. W. Kiefer, (ed.), G. Gouadec, (Guest ed.), Ph. Colomban (Guest ed.), Special issue on the Raman study of nanomaterials. J. Raman Spectr. **38**, 597–796 (2007)
3. G. Turrell, Chap 4: Raman Imaging, in *Raman Microscopy Developments and Applications*, ed. by G. Turrell, J. Corset (Academic Press, London, 1996)
4. Ph. Colomban, Raman analyses and “Smart Imaging" of nanophases and nanosized materials. Spectrosc. Eur. **15**, 8–16 (2003)

5. M. Havel, Ph. Colomban, Smart Raman and Rayleigh Spectroscopy for the analysis of nanomaterials. Microsc. Anal. **20**, 13–15 (2006)
6. Ph. Colomban, Raman Microspectrometry and Imaging of Ceramic Fibers in CMCs and MMCs, in *Advances in Ceramic Matrix Composites V*, ed. by N.P. Bansal, J.P. Singh, E. Ustundag (The American Ceramic Society, Westerville, 2000)
7. M. Baranska, L.M. Proniewicz, Raman mapping of caffeine alkaloid. Vibr. Spectr. **48**, 153–157 (2008)
8. D.W. Piston, Choosing objective lenses: the importance of numerical aperture and magnification in digital optical microscopy. Biol. Bull. **195**, 1–4 (1998)
9. M. Born, E. Wolf, *Principles of Optics* (Pergamon Press, Oxford, 1985)
10. E. Abbe, Archiv. Mikroscopische Anat. **9**, 413 (1873)
11. P.J. Pauzauskie, D. Talaga, K. Seo et al., Polarized Raman confocal microscopy of single gallium nitride nanowires. J. Am. Chem. Soc. **127**, 17146–17147 (2005)
12. D.A. Long, *Raman Spectroscopy* (McGraw-Hill, New York, 1977)
13. M. Delhaye, J. Barbillat, J. Aubard et al., Chap 3: Instrumentation, in *Raman Microscopy Developments and Applications*, ed. by G. Turrell, J. Corset (Academic Press, London, 1996)
14. I. De Wolf, Micro-Raman spectroscopy to study local mechanical stress in silicon integrated circuits. Semicond. Sci. Technol. **11**, 139–154 (1996)
15. G. Turrell, M. Delhaye, P. Dhamelincourt, Chap 2: Characteristics of Raman Microscopy. in *Raman Microscopy Developments and Applications*. (Academic Press, London, 1996)
16. C.J.R. Sheppard, T. Wilson, Depth of field in the scanning microscope. Optics Lett. **3**, 115–117 (1978)
17. C.-B. Juang, L. Finzi, C.J. Bustamante, Design and application of a computer-controlled confocal scanning differential polarization microscope. Rev. Sci. Instrum. **59**, 2399–2408 (1988)
18. V.K. Ramshesh, J.J. Lemasters, Pinhole shifting lifetime imaging microscopy. J. Biomed. Opt. **13**, 064001 (2008)
19. K. Kneipp, M. Moskovits, H. Kneipp, *Surface-Enhanced Raman Scattering*. (Springer, Berlin, 2006)
20. N.P.W. Pieczonka, R.F. Aroca, Single molecule analysis by surface-enhanced Raman scattering. Chem. Soc. Rev. **37**, 946–954 (2008)
21. M. Montagna, R. Dusi, Raman scattering from small spherical particles. Phys. Rev. B **52**, 10080–10089 (1995)
22. A. Roy, A.K. Sood, Growth of CdS_xSe_{1-x} nanoparticles in glass matrix by isochronal thermal annealing: confined acoustic phonons and optical absorptions studies. Solid State Comm. **97**, 97–102 (1996)
23. M. Ferrari, F. Gonella, M. Montagna et al., Detection and size determination of Ag nanoclusters in ion-exchanged soda-lime glasses by waveguided Raman spectroscopy. J. Appl. Phys. **79**, 2055–2059 (1996)
24. V. Paillard, P. Puech, M.A. Laguna et al., Improved one-phonon confinement model for an accurate size determination of silicon nanocrystals. J. Appl. Phys. **86**, 1921–1924 (1999)
25. W.K. Choi, Y.W. Ho, V. Ng, Effect of size of Ge nanocrystals embedded in SiO_2 on Raman spectra. Mater. Phys. Mech. **4**, 46–50 (2001)
26. M. Ivanda, K. Babocsi, C. Dem et al., Low wavenumber Raman scattering from CdS_xSe_{1-x} quantum dots embedded in a glass matrix. Phys. Rev. B **67**, 235329 (2003)
27. K.W. Adu, Q. Xiong, H.R. Gutierrez et al., Raman scattering as a probe of phonon confinement and surface optical modes in semiconducting nanowires. Appl. Phys. **A85**, 287 (2006)
28. M. Ivanda, A. Hohl, M. Montagna et al., Raman scattering of acoustical modes of silicon nanoparticles embedded in silica matrix. J. Raman Spectrosc. **37**, 161 (2006)
29. M. Ivanda, K. Furic, S. Music et al., Low wavenumber Raman scattering of nanoparticle and nanocomposite materials. J. Raman Spectr. **38**, 647–659 (2007)
30. C. Pinghini, D. Aymes, N. Millot et al., Low-frequency Raman characterization of size-controlled anatase TiO_2 nanopowders prepared by continuous hydrothermal syntheses. J. Nanopart. Res. **9**, 309–315 (2007)

31. S.K. Ram, M.N. Islam, S. Kumar et al., Evidence of bimodal crystallite size distribution in μc-Si: H films. Mater. Sci. Eng. A **159–160**, 34–37 (2009)
32. S.K. Gupta, R. Desai, P.K. Jha et al., Titanium dioxide synthesized using Titanium chloride: size effect study using Raman spectroscopy and photoluminescence. J. Raman Spectr. **41**, 350–355 (2010)
33. D. Richards, Near-field microscopy: throwing light on the nanoworld. Phil. Trans. R. Soc. Lond. A **361**, 2843–2857 (2003)
34. E. Bailo, V. Deckert, Tip-enhanced Raman scattering. Chem. Soc. Rev. **37**, 921–930 (2008)
35. B.-S. Yeo, J. Stadler, T. Schmid et al., Tip-enhanced Raman spectroscopy—Its status, challenges and future directions. Chem. Phys. Lett. **472**, 1–13 (2009)
36. N.J. Everall, Confocal Raman microscopy: why the depth resolution and spatial accuracy can be much worse than you think. Appl. Spectr. **54**, 1515–1520 (2000)
37. J.P. Tomba, J.M. Pastor, Confocal Raman microspectroscopy with dry objectives: a depth profiling study on polymer films. Vibr. Spectr. **44**, 62–68 (2007)
38. T. Jawhari, J.C. Merino, J.M. Pastor, Micro-Raman spectroscopy study of the process of microindentation in polymers. J. Mater. Sci. **27**, 2231–2242 (1992)
39. S. Schuckler, S.W. Huffman, I.W. Levin, Vibrational microspectroscopic imaging: spatial resolution enhancement. Proc. SPIE **5321**, 157 (2004)
40. J. Kasim, Y. Ting, Y.Y. Meng et al., Near-field Raman imaging using optically trapped dielectric microsphere. Opt. Express **16**, 7976 (2008)
41. A. Atkinson, S.C. Jain, Spatially resolved stress analysis using Raman spectroscopy. J. Raman Spectrosc. **30**, 885–891 (1999)
42. B. Dietrich, K.F. Dombrowski, Experimental challenges of stress measurements with resonant Micro-Raman spectroscopy. J. Raman Spectrosc. **30**, 893–897 (1999)
43. K. Chikama, K. Matsubara, S. Oyama et al., Three-dimensional confocal Raman imaging of volume holograms formed in ZrO_2 nanoparticle-photopolymer composite materials. J. Appl. Phys. **103**, 113108 (2008)
44. L.-H. He, E.A. Carter, M.V. Swain, Characterization of nanoindentation-induced residual stresses in human enamel by Raman microspectroscopy. Anal. Bioanal. Chem. **389**, 1185–1192 (2007)
45. W.B. White, The structure of particles and the structure of crystals: information from vibrational spectroscopy. J. Ceram. Process. Res. **6**, 1–9 (2005)
46. Ph Colomban, F. Romain, A. Neiman et al., Double Perovskites with oxygen structural vacancies: Raman spectra, conductivity and water uptake. Solid State Ionics **145**, 339–347 (2001)
47. J.E. Spanier, R.D. Robinson, F. Zhang et al., Size-dependent properties of CeO_{2-y} nanoparticles as studied by Raman scattering. Phys. Rev. B **64**, 2450407 (2001)
48. I. Kosacki, T. Suzuki, V. Petrovsky et al., Raman scattering and lattice defects in nanocrystalline CeO_2 thin films. Solid State Ionics **149**, 99–105 (2002)
49. A.V. Gomonnai, Y.M. Azhniuk, V.O. Yukhymchuk et al., Confinement-, surface- and disorder-related effects in the resonant Raman spectra of nanometric $CdS_{1-x}Se_x$ crystals. Phys. Status Solidi B **239**, 490–499 (2003)
50. D. Chiriu, P.C. Ricci, C.M. Carbonaro, Vibrational properties of mixed $(Y_3Al_5O_{12})_x$-$(Y_3Sc_2Ga_3O_{12})_{1-x}$crystals. J. Appl. Phys. **100**, 033101–033105 (2006)
51. Ph Colomban, A. Tournié, L. Bellot-Gurlet, Raman identification of glassy silicates used in ceramic, glass and jewellry: a tentative differentiation guide. J. Raman Spectrosc. **37**, 841–852 (2006)
52. I.H. Campbell, P.M. Fauchet, The effects of mycrocrystal size and shape on the one phonon Raman spectra of crystalline semiconductors. Solid State Comm. **58**, 739–741 (1986)
53. K.R. Patton, M.R. Geller, Phonons in a nanoparticle mechanically coupled to a substrate. Phys. Rev. B **67**(155), 418 (2003)
54. S. Hofmann, C. Ducati, R.J. Neil et al., Gold catalysed growth of silicon nanowires by plasma enhanced chemical vapor deposition. J. Appl. Phys. **94**, 6005–6012 (2003)
55. Q. Xiong, R. Gupta, K.W. Adu et al., Raman spectroscopy and structure of crystalline gallium phosphide nanowires. J. Nanosci. Nanotech. **3**, 335–339 (2003)

56. C. Trallero-Giner, Optical phonons and resonant Raman scattering in II–VI spheroidal quantum dots. Phys. Status Solidi B **241**, 572–578 (2004)
57. A.K. Arora, M. Rajalakshmi, T.R. Ravindran, Phonon Confinement in Nanostructured Materials, in *Encyclopedia of Nanoscience and Nanotechnology*, ed. by H.S. Nalwa (American Scientific Publishers, Valencia, 2004)
58. L. Saviot, D.B. Murray, M.D.C. Marco de Lucas, Vibrations of free and embedded anisotropic elastic spheres: application to low-frequency Raman scattering of silicon nanoparticles in silica. Phys. Rev. B **69**, 113402 (2004)
59. K.-Y. Lee, J.-R. Lim, H. Rho et al., Evolution of optical phonons in CdS nanowires, nanobelts, and nanosheets. Appl. Phys. Lett. **91**, 201901 (2007)
60. A.G. Rolo, M.I. Vasilevskiy, Raman spectroscopy of optical phonons confined in semiconductor quantum dots and nanocrystals. J. Raman Spectr. **38**, 618–633 (2007)
61. Y.-T. Nien, B. Zaman, J. Ouyang et al., Raman scattering for the size of CdSe and CdS nanocrystals and comparison with other techniques. Mater. Lett. **62**, 4522–4524 (2008)
62. S. Pojprapai, J.L. Jones, M. Hoffman, Determination of domain orientation in Lead Zirconate Titanate ceramics by Raman spectroscopy. Appl. Phys. Lett. **88**, 162903 (2006)
63. M. Deluca, T. Sakashita, G. Pezzotti, Polarized Raman scattering of domain structures in polycrystaline Lead Zirconate Titanate. Appl. Phys. Lett. **90**, 051919 (2007)
64. M. Becker, H. Scheel, S. Christiansen et al., Grain orientation, texture, and internal stress optically evaluated by micro-Raman spectroscopy. J. Appl. Phys. **101**, 063531 (2007)
65. D.B. Murray, C.H. Netting, R.B. Mercer et al., Polarizability calculation of vibrating nanoparticles for intensity of low wavenumber Raman scattering. J. Raman Spectr. **38**, 770–779 (2007)
66. H.M. Fan, X.F. Fan, Z.H. Ni et al., Orientation-dependant Raman spectroscopy of single Wurtzite CdS nanowires. J. Phys. Chem. C **112**, 1865–1870 (2008)
67. C. Galiotis, Laser Raman spectroscopy, a new stress/strain measurement technique for the remote and online non-destructive inspection of fiber reinforced polymer composites. Mater. Technol. **8**, 203–209 (1993)
68. L.S. Schadler, C. Galiotis, Fundamentals and applications of micro Raman spectroscopy to strain measurements in fibre reinforced composites. Inter. Mater. Rev. **40**, 116–134 (1995)
69. E. Anastassakis, Selection rules of Raman scattering by optical phonons in strained cubic crystals. J. Appl. Phys. **82**, 1582–1591 (1997)
70. G. Lucazeau, Effect of pressure and temperature on Raman spectra of solids: anharmonicity. J. Raman Spectrosc. **34**, 478–496 (2003)
71. D. Bollas, J. Parthenios, C. Galiotis, Effect of stress and temperature on the optical phonons of aramid fibers. Phys. Rev. B **73**, 094103 (2006)
72. H. Richter, Z.P. Wang, L. Ley, The one phonon Raman spectrum in microcrystalline silicon. Solid State Comm. **39**, 625–629 (1981)
73. P. Parayanthal, F.H. Pollak, Raman scattering in alloy semiconductors: "spatial correlation" model. Phys. Rev. Lett. **52**, 1822–1825 (1984)
74. H. Lamb, On the vibrations of an elastic sphere. Proc. London Math. Soc. **13**, 189–212 (1882)
75. A. Tamura, K. Higeta, T. Ichinokawa, Lattice vibrations and specific heat of a small particle. J. Phys. C: Solid State Phys. **15**, 4975–4991 (1982)
76. E. Duval, Far-Infrared and Raman vibrational transitions of a solid sphere: selection rules. Phys. Rev. B **46**, 5795–5797 (1992)
77. A. Tanaka, S. Onari, T. Arai, Low-frequency Raman scattering from CdS microcrystals embedded in a Germanium Dioxide glass matrix. Phys. Rev. B **47**, 1237–1243 (1993)
78. L. Saviot, D.B. Murray, The connection between elastic scattering cross sections and acoustic vibrations of an embedded nanoparticle. Phys. Status Solidi C **1**, 2634–2637 (2004)
79. E. Duval, A. Boukenter, B. Champagnon, Vibration eigenmodes and size of microcrystallites in glass: observation by very-low-frequency Raman scattering. Phys. Rev. Lett. **56**, 2052–2055 (1986)
80. P. Verma, W. Cordts, G. Irmer et al., Acoustic vibrations of semiconductor nanocrystals in doped glasses. Phys. Rev. B **60**, 5778–5785 (1999)

81. M.C. Klein, F. Hache, D. Ricard et al., size dependence of electron–phonon coupling in semiconductor nanospheres: the case of CdSe. Phys. Rev. B **42**, 11123–11132 (1990)
82. F. Comas, C. Trallero-Giner, N. Studart et al., Interface optical phonons in spheroidal dots: Raman selection rules. Phys. Rev. B **65**, 073303 (2002)
83. E.P. Pokatilov, S. Klimin, V.M. Fomin et al., Multi-phonon Raman scattering in semiconductor nanocrystals: importance of non-adiabatic transitions. Phys. Rev. B **65**, 075316 (2002)
84. M.I. Vasilevskiy, Dipolar vibrational modes in spherical semiconductor quantum dots. Phys. Rev. B **66**, 195326 (2002)
85. V.A. Fonoberov, A.A. Balandin, Polar optical phonons in Wurtzite spheroidal quantum dots: theory and application to ZnO and ZnO/MgZnO nanostructures. J. Phys. Cond. Matter **17**, 1085–1097 (2005)
86. Q.H. Zhong, Optical phonon modes in a free-standing quantum wire with ring geometry. Phys. Lett. A **372**, 5932–5937 (2008)
87. H. Shinzawa, K. Awa, W. Kanematsu et al., Multivariate data analysis for Raman spectroscopic imaging. J. Raman Spectr. **40**, 1720–1725 (2009)
88. I. Noda, Generalized two-dimensional correlation method applicable to infrared, Raman, and other types of spectroscopy. Appl. Spectrosc. **47**, 1329–1336 (1993)
89. Y.M. Jung, I. Noda, New approaches to generalized two-dimensional correlation spectroscopy and its applications. Appl. Spectr. Rev. **41**, 515–547 (2006)
90. M.A. Czarnecki, Interpretation of two-dimensional correlation spectra: science or art? Appl. Spectrosc. **52**, 1583–1590 (1998)
91. M.A. Czarnecki, Two-dimensional correlation spectroscopy: effect of normalization of the dynamic spectra. Appl. Spectrosc. **53**, 1392–1397 (1999)
92. G. Gouadec, J.-P. Forgerit, Ph Colomban, Choice of the working conditions for Raman extensometry of carbon and SiC fibers by 2D correlation. Comp. Sci. Technol. **62**, 505–511 (2002)
93. C. Thomsen, S. Reich, Double resonant Raman scattering in graphite. Phys. Rev. Lett. **85**, 5214–5217 (2000)
94. F. Tuinstra, J.L. Koenig, Raman spectrum of graphite. J. Chem. Phys. **53**, 1126–1130 (1970)
95. A.C. Ferrari, J. Robertson, Interpretation of Raman spectra of disordered and amorphous carbon. Phys. Rev. B **61**, 14095–14107 (2000)
96. R. Carles, A. Mlayah, M.B. Amjoud et al., Structural characterization of Ge microcrystals in Ge_xC_{1-x} films. Jap. J. Appl. Phys. **31**(pt 1), 3511–3514 (1992)
97. Y.K. Kim, H.M. Jang, Raman lineshape analysis of nano-structural evolution in cation—ordered $ZrTiO_4$—based dielectrics. Solid State Comm. **127**, 433–437 (2003)
98. A.K. Arora, M. Rajalakshmi, T.R. Ravindran et al., Raman spectroscopy of optical phonon confinement in nanostructured materials. J. Raman Spectr. **38**, 604–617 (2007)
99. M. Havel, Ph Colomban, Skin/Bulk nanostructure and corrosion of SiC based fibres. A surface Rayleigh and Raman study. J. Raman Spectrosc. **34**, 786–794 (2003)
100. M. Havel, Ph. Colomban, Rayleigh and Raman images of the bulk/surface nanostructure of SiC based fibres. Compos. Part B. **35**, 139–147 (2004)
101. M. Havel, D. Baron, Ph Colomban, Smart Raman/Rayleigh imaging of nanosized SiC materials using the spatial correlation model. J. Mater. Sci. **39**, 6183–6190 (2004)
102. A. Tanaka, S. Onari, T. Arai, Raman scattering from CdS microcrystals embedded in a Germanate glass matrix. Phys. Rev. B **45**, 6587–6592 (1992)
103. J. Zuo, C. Xu, Y. Liu et al., Crystallite size effects on the Raman spectra of Mn_3O_4. Nanostruct. Mater. **10**, 1331–1335 (1998)
104. K.K. Tiong, P.M. Amirtharaj, F.H. Pollak et al., Effects of As^+ ion implantation on the Raman spectra of GaAs: "Spatial Correlation" interpretation. Appl. Phys. Lett. **44**, 122–124 (1984)
105. J. Zuo, C. Xu, B. Hou et al., Raman spectra of nanophase Cr_2O_3. J. Raman Spectrosc. **27**, 921–923 (1996)
106. A. Fischer, L. Anthony, A.D. Compaan, Raman analysis of short-range clustering in Laser—Deposited CdS_xTe_{1-x} Films. Appl. Phys. Lett. **72**, 2559–2561 (1998)
107. W.F. Zhang, Y.L. He, M.S. Zhang et al., Raman scattering study on anatase TiO_2 nanocrystals. J. Phys. D **33**, 912–916 (2000)

108. Y.K. Kim, H.M. Jang, Polarization leakage and asymmetric Raman line broadening in microwave dielectric $ZrTiO_4$. J. Phys. Chem. Solids **64**, 1271–1278 (2003)
109. H.M. Jang, T.-Y. Kim, I.-W. Park, Nano-sized clusters with tetragonal symmetry in $PbTiO_3$—based relaxor ferroelectrics. Sol. State Comm. **127**, 645–648 (2003)
110. R.S. Chen, C.C. Chen, Y.S. Huang et al., A comparative study of microstructure of RuO_2 nanorods via Raman scattering and field emission scanning electron microscopy. Sol. State Comm. **131**, 349–353 (2004)
111. X.J. Ning, P. Pirouz, The microstructure of SCS-6 SiC fibre. J. Mater. Res. **6**, 2234–2248 (1991)
112. A.B. Mann, M. Balooch, J.H. Kinney et al., Radial variations in modulus and hardness in SCS-6 silicon carbide fibers. J. Am. Ceram. Soc. **82**, 111–116 (1999)
113. M. Havel, D. Baron, L. Mazerolles et al., Phonon confinement in SiC nanocrystals: comparison of the size determination using transmission electron microscopy and Raman spectroscopy. Appl. Spectrosc. **61**, 855–859 (2007)
114. S. Ganesan, A.A. Maradudin, J. Oitmaa, A lattice theory of morphic effects in crystals of the diamond structure. Ann. Phys. **56**, 556–594 (1970)
115. E. Anastassakis, A. Pinczuk, E. Burnstein et al., Effect of static uniaxial stress on the Raman spectrum of silicon. Solid State Comm. **8**, 133–138 (1970)
116. E. Anastassakis, Inelastic light scattering in the presence of uniaxial stress. J. Raman Spectr. **10**, 64–76 (1981)
117. I. De Wolf, H.E. Maes, S.K. Jones, Stress measurements in silicon devices through Raman spectroscopy: bridging the gap between theory and experiment. J. Appl. Phys. **79**, 7148–7156 (1996)
118. I. De Wolf, Stress measurements in Si microelectronics devices using Raman spectroscopy. J. Raman Spectrosc. **30**, 877–883 (1999)
119. I. De Wolf, Raman spectroscopy: about chips and stress. Spectroscopy Europe **15**, 6–13 (2002)
120. J. Wu, Ph Colomban, Raman spectroscopy study on the stress distribution in the continuous Fibre-reinforced CMC. J. Raman Spectrosc. **28**, 523–529 (1997)
121. G. Gouadec, S. Karlin, Ph. Colomban, Raman Extensometry Study of NLM202 and Hi-Nicalon SiC Fibres. Compos. Part B **29**, 251–261 (1998)
122. B. Mottershead, S.J. Eichhorn, Deformation micromechanics of model regenerated cellulose fibre-epoxy/polyester composites. Comp. Sci. & Tech. **67**, 2150–2159 (2007)
123. W.T.Y. Tze, S.C. O'Neill, C.P. Tripp et al., Evaluation of load transfer in the cellulosic–fiber/polymer interphase using a micro-Raman tensile test. Wood and Fiber Sci. **39**, 184–195 (2007)
124. L. Zhenkun, Q. Wei, K. Yilan et al., Stress transfer of single fiber/microdroplet tensile test studied by micro-Raman spectroscopy. Compos. Part A **39**, 113–118 (2008)
125. C. Galiotis, A. Paipetis, C. Marston, Unification of fibre/matrix interfacial measurements with Raman microscopy. J. Raman Spectrosc. **30**, 899–912 (1999)
126. A. Paipetis, C. Galiotis, Y.C. Liu et al., Stress-transfer from the matrix to the fibre in a fragmentation test: Raman experiments and analytical modeling. J. Comp. Mater. **33**, 377–399 (1999)
127. E. Pisanova, S. Zhandarov, E. Mäder et al., Three techniques of interfacial bond strength estimation from direct observation of crack initiation and propagation in polymer–fibre systems. Compos. Part A **32**, 435–443 (2001)
128. R.J. Young, C. Thongpin, J.L Stanford et al., Fragmentation analysis of glass fibres in model composites through the use of Raman spectroscopy. Compos. Part A **32**, 253–269 (2001)
129. P.I. Gonzalez-Chi, R.J. Young, Deformation micromechanics of a thermoplastic–thermoset interphase of epoxy composites reinforced with polyethylene fiber. J. Mater. Sci. **39**, 7049–7059 (2004)
130. G. Anagnostopoulos, A.G. Andreopoulos, J. Parthenios et al., Global method for measuring stress in polymer fibers at elevated temperatures. Appl. Phys. Lett. **87**, 131910 (2005)
131. G. Anagnostopoulos, J. Parthenios, A.G. Andreopoulos et al., An experimental and theoretical study of the stress transfer problem in fibrous composites. Acta Mater. **53**, 4173–4183 (2005)

132. A.B. Coffey, C.M. O'Bradaigh, R.J. Young, Interfacial stress transfer in an aramid reinforced thermoplastic elastomer. J. Mater. Sci. **42**, 8053–8061 (2006)
133. R. Kumar, S.B. Cronin, Optical properties of carbon nanotubes under axial strain. J. Nanosci. Nanotech. **8**, 1–9 (2007)
134. J.R. Wood, Q. Zhao, M.D. Frogley et al., Carbon nanotubes: from molecular to macroscopic sensors. Phys. Rev. B **62**, 7571–7575 (2000)
135. Q. Zhao, M.D. Frogley, H.D. Wagner, The use of carbon nanotubes to sense matrix stress around a single glass fiber. Comp. Sci. Technol. **61**, 2139–2143 (2001)
136. Q. Zhao, M.D. Frogley, H.D. Wagner, Direction-sensitive stress measurements with carbon nanotubes sensors. Polym. Adv. Techn. **13**, 759–764 (2002)
137. C.A. Cooper, R.J. Young, M. Halsall, Investigation into the deformation of carbon nanotubes and their composites through the use of Raman spectroscopy. Compos. Part A **32**, 401–411 (2001)
138. M.S. Dresselhaus, G. Dresselhaus, R. Saito et al., Raman spectroscopy of carbon nanotubes. Phys. Rep. **409**, 47–99 (2005)
139. C. Thomsen, S. Reich, Chap 3: Raman Scattering in Carbon Nanotubes. in *Light Scattering in Solids IX: Novel Materials and Techniques*, ed. by M. Cardona, R. Merlin (Springer, Heidelberg, 2006)
140. V. Domnich, Y. Aratyn, W.M. Kriven et al., Temperature Dependance of silicon hardness: experimental evidence of phase transformations. Rev. Adv. Mater. Sci **17**, 33–41 (2008)
141. C.R. Das, H.C. Hsu, S. Dhara et al., A complete Raman mapping of phase transitions in Si under indentation. J. Raman Spectr. **41**, 334–339 (2010)
142. S. Kouteva-Arguirova, V. Orlov, W. Seifert et al., Raman investigation of stress and phase transformation induced in silicon by indentation at high temperatures. Eur. Phys. J. Appl. Phys. **27**, 279–283 (2004)
143. P. Puech, F. Demangeot, J. Frandon et al., GaN nanoindentation: a micro-Raman spectroscopy study of local strain fields. J. Appl. Phys. **96**, 2853–2856 (2004)
144. N. Orlovskaya, D. Steinmetz, S. Yarmolenko et al., Detection of temperature- and stress-induced modifications of $LaCoO_3$ by micro-Raman spectroscopy. Phys. Rev. B **72**, 014122 (2005)
145. T. Wermelinger, C. Borgia, C. Solenthaler et al., 3-D Raman spectroscopy measurements of the symmetry of residual stress fields in plastically deformed sapphire crystals. Acta Mater. **55**, 4657–4665 (2007)
146. C.R. Das, S. Dhara, H.C. Hsu et al., The mechanism of the recrystallization process in epitaxial GaN under dynamic stress field: atomistic origin of planar defect formation. J. Raman Spectr. **40**, 1881–1884 (2009)
147. Y.B. Gerbig, S.J. Stranick, D.J. Morris et al., Effect of crystallographic orientation on phase transformations during indentation of silicon. J. Mater. Res. **24**, 1172–1183 (2009)
148. T. Wermelinger, R. Spolenak, Correlating Raman peak shifts with phase transformation and defect densities: a comprehensive TEM and Raman study on silicon. J. Raman Spectr. **40**, 679–686 (2009)
149. Ph Colomban, M. Havel, Raman imaging of stress-induced phase transformation in transparent ZnSe ceramics and Sapphire single crystal. J. Raman Spectrosc. **33**, 789–795 (2002)
150. D. Neff, S SR, L. Bellot-Gurlet et al., Structural characterization of corrosion products on archaeological iron: an integrated analytical approach to establish corrosion forms. J. Raman Spectrosc. **35**, 739–745 (2004)
151. S. Réguer, D. Neff, L. Bellot-Gurlet et al., Deterioration of iron archaeological artefacts: micro-Raman investigation on Cl-containing corrosion products. J. Raman Spectrosc. **38**, 389–397 (2007)
152. L. Bellot-Gurlet, D. Neff, S. Réguer et al., Raman studies of corrosion layers formed on archaeological irons in various media. J. Nano Res. **8**, 147–156 (2009)
153. Ph Colomban, S. Cherifi, G. Dexpert, Raman identification of corrosion products on automotive galvanized steel sheets. J. Raman Spectr. **39**, 881–886 (2008)

154. P. Dillmann, G. Béranger, P. Piccardo et al. (eds). *Corrosion of Metallic Heritage Artefacts. Investigation, Conservation and Prediction for Long-Term Behaviour*, European federation of corrosion publications-EFC, vol. 48 (Woodhead, Cambridge, 2007)
155. D. Neff, L. Bellot-Gurlet, P. Dillmann et al., Raman imaging of ancient rust scales on archaeological iron artefacts for long-term atmospheric corrosion mechanisms study. J. Raman Spectrosc. **37**, 1228–1237 (2006)
156. H. Antony, S. Perrin, P. Dillmann et al., Electrochemical study of indoor atmospheric corrosion layers formed on ancient iron artefacts. Electrochimica Acta **52**, 7754–7759 (2007)
157. Monnier J (2008) Corrosion Atmosphérique sous Abri d'Alliages Ferreux Historiques. Caractérisation du Système, Mécanismes et Apport à la Modélisation, Ph.D Thesis, Université Paris-Est (http://tel.archives-ouvertes.fr/tel-00369510/fr/)
158. J. Monnier, L. Legrand, L. Bellot-Gurlet et al., Study of archaeological artefacts to refine the model of iron long-term indoor atmospheric corrosion. Journal of Nuclear Materials **379**, 105–111 (2008)
159. J. Monnier, L. Bellot-Gurlet, D. Baron et al., A methodology for Raman structural quantification imaging and its application to iron indoor atmospheric corrosion products. J. Raman Spectrosc. **42**, 773–781 (2011)
160. S. Bernad, T. Soulimane, S. Lecomte, Redox and conformational equilibria of cytochrome c_{552} from thermus thermophilus adsorbed on chemically modified silver electrode probed by SERS. J. Raman Spectrosc. **35**, 47–54 (2004)
161. F. Salpin, F. Trivier, S. Lecomte et al., A new quantitative method: non-destructive study by Raman spectroscopy of dyes fixed on wool fibres. J. Raman Spectrosc. **37**, 1403–1410 (2006)
162. F. Dubois, C. Mendibide, T. Pagnier et al., Raman mapping of corrosion products formed onto spring steels during salt spray experiments. A correlation between the scale composition and the corrosion resistance. Corros. Sci. **50**, 3401–3409 (2008)
163. S. Keren, C. Zavaleta, Z. Cheng et al., Noninvasive molecular imaging of small living subjects using Raman spectroscopy. PNAS **105**, 5844–5849 (2008)
164. A. Beljebbar, O. Bouché, M.D. Diébold et al., Identification of Raman spectroscopic markers for the characterization of normal and adenocarcinomatous colonic tissues. Crit. Rev. Oncol. Hematol. **72**, 255–264 (2009)
165. B.R. Lutz, C.E. Dentinger, L.N. Nguyen et al., Spectral analysis of multiplex Raman probe signatures. ACS Nano **2**, 2306–2314 (2008)